

RICE UNIVERSITY

Terahertz imaging with compressive sensing

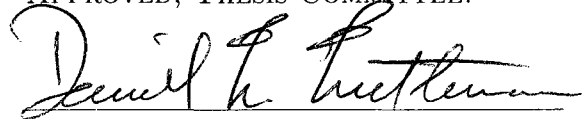
by

Wai Lam Chan

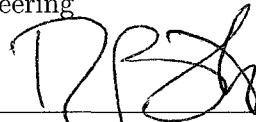
A THESIS SUBMITTED
IN PARTIAL FULFILLMENT OF THE
REQUIREMENTS FOR THE DEGREE

Doctor of Philosophy

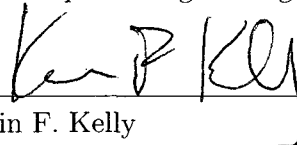
APPROVED, THESIS COMMITTEE:



Daniel M. Mittleman, Chair
Professor of Electrical and Computer
Engineering



Richard G. Baraniuk
Victor E. Cameron Professor of Electrical
and Computer Engineering



Kevin F. Kelly
Associate Professor of Electrical and
Computer Engineering



Wotao Yin
Assistant Professor of Computational and
Applied Mathematics

Houston, Texas

April, 2010

UMI Number: 3421392

All rights reserved

INFORMATION TO ALL USERS

The quality of this reproduction is dependent upon the quality of the copy submitted.

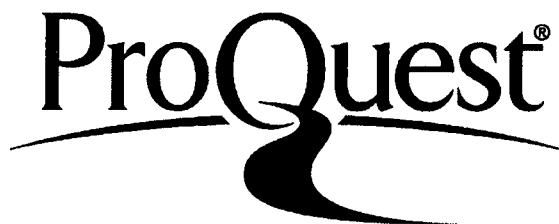
In the unlikely event that the author did not send a complete manuscript and there are missing pages, these will be noted. Also, if material had to be removed, a note will indicate the deletion.



UMI 3421392

Copyright 2010 by ProQuest LLC.

All rights reserved. This edition of the work is protected against unauthorized copying under Title 17, United States Code.



ProQuest LLC
789 East Eisenhower Parkway
P.O. Box 1346
Ann Arbor, MI 48106-1346

ABSTRACT

Terahertz imaging with compressive sensing

by

Wai Lam Chan

Most existing terahertz imaging systems are generally limited by slow image acquisition due to mechanical raster scanning. Other systems using focal plane detector arrays can acquire images in real time, but are either too costly or limited by low sensitivity in the terahertz frequency range.

To design faster and more cost-effective terahertz imaging systems, the first part of this thesis proposes two new terahertz imaging schemes based on compressive sensing (CS). Both schemes can acquire amplitude and phase-contrast images efficiently with a single-pixel detector, thanks to the powerful CS algorithms which enable the reconstruction of N -by- N pixel images with much fewer than N^2 measurements. The first CS Fourier imaging approach successfully reconstructs a 64×64 image of an object with pixel size 1.4 mm using a randomly chosen subset of the 4096 pixels which defines the image in the Fourier plane. Only about 12% of the pixels are required for reassembling the image of a selected object, equivalent to a $2/3$ reduction in acquisition time. The second approach is single-pixel CS imaging, which uses a series of random masks for acquisition. Besides speeding up acquisition with a reduced number of measurements, the single-pixel system can further cut down acquisition time by electrical or optical spatial modulation of random patterns.

In order to switch between random patterns at high speed in the single-pixel

imaging system, the second part of this thesis implements a multi-pixel electrical spatial modulator for terahertz beams using active terahertz metamaterials. The first generation of this device consists of a 4×4 pixel array, where each pixel is an array of sub-wavelength-sized split-ring resonator elements fabricated on a semiconductor substrate, and is independently controlled by applying an external voltage. The spatial modulator has a uniform modulation depth of around 40 percent across all pixels, and negligible crosstalk, at the resonant frequency. The second-generation spatial terahertz modulator, also based on metamaterials with a higher resolution (32×32), is under development. A FPGA-based circuit is designed to control the large number of modulator pixels. Once fully implemented, this second-generation device will enable fast terahertz imaging with both pulsed and continuous-wave terahertz sources.

Acknowledgments

Graduate school life is adventurous. It has not been easy to always keep up the enthusiasm towards research. However, a lot of support from the academic community at Rice University has strengthened me to climb one mountain after another. I would like to thank my advisor, professor Daniel Mittleman, who always has brilliant and inspiring research ideas. At the same time, he is very understanding and kind to his students. Thanks to my committee members, professor Richard Baraniuk for encouraging me to pursue research in terahertz, professor Kevin Kelly for promoting the ideas of single-pixel imaging to terahertz, and professor Wotao Yin for patiently explaining to me the ideas behind the fast reconstruction algorithms. When designing the circuit boards for my last project, I receive much help from professor Gary Woods, Siddharth Gupta and Patrick Murphy. They have taught me what a real electrical engineer should know, and I feel very satisfied after putting all the components together to work.

Words are not enough to express my thanks towards my parents, who have sacrificed so much to provide the financial support for my studies in the US. They pray for me constantly, and love me even though I am not always nice on the phone, especially during stressful times. During this past year finishing up my degree while working a full-time job, my girlfriend, Emily, cares for me, makes gifts for me and cooks for me. With my heart, I sincerely appreciate what she has done and I will continue to learn how to love her. My friends, no matter in the US or in Hong Kong, have also given me tremendous emotional and spiritual support. In particular, I am grateful for Bryan, who has come from Hong Kong to visit me twice in Houston, and for Matthew, who is always available when I need a listening ear. My friends from church and tennis

buddies have also made my graduate school life more fun.

Finally, many thanks and praises to God. He has created this awesome universe for me to discover, yet He loves me so much that He has died for me on the cross. I am very thankful for the talent and the opportunities which He has given me, all the difficult times which He has brought me through, and all the wonderful relationships He has prepared in my life.

Contents

Abstract	ii
Acknowledgments	iv
List of Illustrations	ix
1 Introduction	1
1.1 Terahertz imaging and compressive sensing	3
1.2 Scope of this thesis	4
2 Background	6
2.1 Terahertz imaging	6
2.1.1 Time-domain terahertz system	6
2.1.2 Imaging with a time-domain spectrometer	11
2.1.3 Other imaging methods	14
2.1.4 Terahertz imaging applications	17
2.2 Compressive sensing (CS)	17
2.2.1 CS background	17
2.2.2 CS imaging applications	21
3 A CS Fourier terahertz imaging system	22
3.1 Imaging setup	22
3.2 Experimental results	23
3.2.1 Fourier reconstruction with full dataset	23
3.2.2 CS reconstruction with partial dataset	24
3.2.3 CS and phase retrieval	27

3.3	Discussion	29
4	A Single-pixel CS terahertz imaging system	31
4.1	CS imaging principle	32
4.2	Imaging experiment	33
4.3	Imaging results: Amplitude-only images	35
4.4	Imaging results: Complex images	37
4.5	Discussion	39
5	Terahertz spatial light modulator (SLM)	40
5.1	Metamaterials	41
5.2	First-generation 4×4 SLM design	42
5.3	Experiments and results	43
5.3.1	Modulation depth	44
5.3.2	Crosstalk	45
5.3.3	Switching performance	46
5.4	Second-generation 32×32 SLM design	48
5.5	Characterization experiments and results	49
5.6	Discussion	51
6	A future CS terahertz imaging system	56
6.1	Summary of results	56
6.2	Future challenges	58
6.2.1	Terahertz SLM technology	58
6.2.2	Terahertz source power and receiver dynamic range	59
6.2.3	Terahertz spectroscopic and phase imaging	61
A	Implementation of minimization of total variation (min-TV) algorithm	63

B Second-generation terahertz SLM control system	65
B.1 FPGA circuit	66
B.2 FPGA Verilog programming	69
B.3 FPGA pin assignments	70
B.4 Line driver circuit	71
B.5 SLM board	75
B.6 Auxiliary components	79
B.7 Synchronization with T-ray system	80
B.8 System test procedure	81
Bibliography	83

Illustrations

- 1.1 *The terahertz region of the spectrum lies between microwaves and infrared, and is characterized by a free-space wavelength between 30 microns and 3 millimeters. The photon energy corresponding to $k_B T$ at room temperature, 40 meV, is equivalent to a frequency of about 10 THz. 2*

- 2.1 *One of the first images acquired using a time-domain system, adapted from the original paper by Hu and Nuss. This shows a transmission image of a semiconductor integrated circuit, through the black epoxy package which is transparent to terahertz radiation. The metallization inside the package is clearly visible, as is the semiconductor wafer in the center. The spatial resolution of this image is roughly 250 microns. The inset shows an optical image of the sample. 7*

- 2.2 (left) A typical time-domain terahertz waveform, measured in ambient air. The oscillatory features which follow the initial single-cycle transient are the result of water vapor in the beam path. The dotted curve shows the intensity envelope, computed from the measured electric field $E(t)$ using a Hilbert transform. (right) The spectral amplitude $|E(\omega)|$ derived from the field shown at left by Fourier transform, on a log scale. The vertical arrows indicate the spectral positions of tabulated water vapor absorption lines. The inset shows the spectral phase, also derived from the time-domain measurement. This is essentially linear, as expected for a single-cycle pulse. The effects of the water vapor absorption lines on the phase are measurable, but are too small to see in this display. 9
- 2.3 A schematic of a typical transmission-mode raster-scan time-domain imaging system. 12
- 3.1 The THz Fourier imaging setup. An approximately collimated beam from the THz transmitter illuminates an object mask, placed one focal length away from the focusing lens. The THz receiver raster-scans and samples the Fourier transform of the object on the focal plane. 23

- 3.2 *Compressed sensing imaging results. (a) Magnitude of image reconstructed by inverse Fourier transform using the full data set (4096 uniformly sampled measurements), and (d) its phase. Note the phase distortion inherent in the THz beam in (d). Compressed sensing reconstruction result using 500 measurements (12%) from the full data set: (b) magnitude, and (e) phase. Compressed sensing with phase correction improves image quality and eliminates phase distortion (see (c) and (f)). All figures show a zoom-in view on a 40×40 grid centered on the object. 25*
- 3.3 *Comparison of quality of image reconstruction between CS with and without phase correction. As the number of measurements (M) used in CS increases, the mean-squared error (MSE) between the magnitudes of the reconstructed image and the reference image (see Fig 3.2(a)), normalized by the energy of the reference image, decreases. CS with phase correction shows superior reconstruction performance. 27*
- 3.4 *Image reconstruction results using (a) compressive phase retrieval (CPR) with the full data set (4096 magnitude measurements), and (b) compressed sensing phase retrieval (CSPR) with a subset of 1500 measurements from the data set used in (a). 28*
- 4.1 *The THz compressive imaging setup. An approximately collimated beam from the THz transmitter illuminates an object mask and is partially ($\sim 50\%$) transmitted through a random pattern of opaque pixels. The random patterns, the focusing lens and the receiver are placed in order to most efficiently focus the THz beam onto the receiver antenna. One complete time-domain waveform is collected for each random pattern. 33*

- 4.2 (a) White-light image of object mask shaped as the Chinese character "light". Terahertz images reconstructed via compressed sensing using (b) 300 and (c) 600 magnitude measurements, which are respectively about 30% and 60% of the total number of image pixels. Both figures display a 32×32 image and the pixel size is $1\text{mm} \times 1\text{mm}$ 35
- 4.3 As the number of measurements (M) used in CS increases, the mean-squared error (MSE) between the magnitudes of the reconstructed image and the reference image for the object in Figure 4.2, normalized by the squared energy of the reference image, decreases. The MSE decay is fast from 50 to 100 CS measurements. After the number of CS measurements exceeds the "sparsity" of the object, the decay flattens out. 36
- 4.4 Compressed sensing reconstructions of (a) the image amplitude and (b) the phase, using 400 (complex) measurements. Here, the object is a rectangular hole in an opaque screen, covered with a (transparent) plastic plate. The plate covering the upper half of the hole is thicker than the lower half. The reconstructed phase image exhibits this contrast much better than the amplitude image. 37
- 4.5 The estimated thickness of the plastic plate, versus number of measurements (n) used in CS reconstruction for the object in Figure 4.4. Dashed line indicates the actual thickness difference (1.73 mm), as determined using a micrometer. The thickness estimates rapidly converge to the correct answer with increasing n 38

- 5.1 (a) Each single pixel on the THz SLM contains a $4 \times 4 \text{ mm}^2$, ~ 2500 element array of metamaterial SRRs. These elements are connected together with metal wires to serve as a metallic (Schottky) gate. An external voltage bias controls the substrate charge carrier density near the split gaps, tuning the strength of the resonance. (b) Diagram of the substrate and the depletion region near the split gap of a single SRR, where the gray scale indicates the free charge carrier density. (c) The THz SLM (not drawn to scale) is a 4×4 array of individual pixels in (a). Each pixel is independently controlled by an external voltage between the $1 \times 1 \text{ mm}^2$ Schottky electric pad and the ohmic contact. 43
- 5.2 (a) THz amplitude transmission spectra for one of the 16 pixels of the THz SLM without voltage bias (dashed) and with 14V bias (solid). A large modulation depth is observed at 0.36 THz, the design resonant frequency. (b) A transmission image of the 4-by-4 array at 0.36 THz, with two pixels turned off (biased), and the rest turned on (zero bias). 44
- 5.3 Noise-to-signal power ratio (dashed) and noise-plus-crosstalk-to-signal power ratio (dotted) across frequency, from which we obtain the crosstalk level (solid). Above 0.33 THz (in the shaded area), crosstalk is buried in noise, and is therefore unmeasurable. These ratios are calculated from their corresponding transmission images of the 4-by-4 array of the THz SLM at every frequency. In the inset image at 0.36 THz, two pixels are under a square voltage bias and the rest are unbiased. A THz modulation (differential) signal is measured at each pixel using the lock-in amplifier referenced to the square voltage. . . . 46

- 5.4 Measured (solid curves) differential fringe patterns produced by the transmission of the THz beam through the THz SLM in two double-slit configurations, compared with analytical calculations (dashed curves). The insets show the “on” and “off” configurations of the 16 pixels, with zero bias on the gray pixels, and the white pixels modulated with a 3-kHz square signal alternating between 0 and 14V. 47
- 5.5 (a) The second-generation terahertz SLM is a 32×32 array of individual pixels in Figure 5.6(a). Each pixel is independently controlled by an external voltage between the respective Schottky electric pad and the ohmic contacts (L-shaped pads at the four corners). The 256 Schottky pads on each side control all the pixels in one quadrant (triangular-shaped). (b) The active area of each pixel is $880 \mu\text{m} \times 860 \mu\text{m}$ and the spacing between pixels is about $200 \mu\text{m}$. The connecting wires between the pixels are $6 \mu\text{m}$ in width and $4 \mu\text{m}$ apart. 49
- 5.6 Geometry of (a) one SLM pixel and (b) one metamaterial SRR element of the SLM. Each single pixel ($880 \mu\text{m} \times 860 \mu\text{m}$) contains a 10×10 element array of metamaterial SRRs. Each SRR element is $88 \mu\text{m} \times 86 \mu\text{m}$, with $6 \mu\text{m}$ -wide metal and $2 \mu\text{m}$ split gaps. 50
- 5.7 Frequency-dependent terahertz transmission amplitude for a typical terahertz SLM pixel at various reverse gate biases for terahertz polarization (a) parallel to and (b) perpendicular to the connecting wires. Maximum modulation observed is 25% at 0.42 THz in (a) and is 20% at 0.37 THz in (b). 51

5.8 (a) Locations of defects on SLM 1 observed under the microscope (see lines sketched on mask). (b) An 32×32 image of the modulation depth of the pixels on SLM 1, overlaid with sketches of defects in (a). At 0.37 THz, the SLM provides around 20% amplitude modulation at the darker regions on the image, and has zero modulation at the brighter regions. The defects cut off some SLM pixels from their Schottky pads, thus the SLM cannot provide any amplitude modulation at the corresponding pixel locations. 53

5.9 Microscope images of defect locations on SLM 1 indicated on Figure 5.8(a). Location 1 has a crack whereas location 2 and 3 have fabrication defects. 54

5.10 (a) Locations of defects on SLM 2 observed under the microscope (see lines sketched on mask). (b) An 32×32 image of the modulation depth of the pixels on SLM 2, overlaid with sketches of defects in (a). At 0.37 THz, the SLM provides around 20% amplitude modulation at the darker regions on the image, and has zero modulation at the brighter regions. The defects cut off some SLM pixels from their Schottky pads, thus the SLM cannot provide any amplitude modulation at the corresponding pixel locations. 54

5.11 Microscope images of defect locations on SLM 2 indicated on Figure 5.10(a). A continuous crack runs through location 1 and 2 on SLM 2. 55

6.1 Comparison of CS imaging systems with raster-scan and detector array systems. Assuming system implementation with a continuous-wave THz source, the single-pixel imaging system can provide high-speed imaging at room temperature with a reasonable hardware requirement. 61

- A.1 *Test FTVd reconstruction results of the Chinese character “light” for the single-pixel CS imaging system for various μ and a maximum β of 1024. A smaller μ yields a smoother image while a larger μ gives a sharper but noisier image. 64*
- B.1 *Terahertz SLM control system diagram. The control system consists of three circuit boards: the FPGA platform which controls the switching of each SLM pixels and the synchronization between the SLM and the T-ray system, two line driver boards which increase the voltage amplitude of each switching signal from 3V to 16V, and the SLM board which holds the SLM chip. 67*
- B.2 *Xilinx AFX-FF1760 FPGA prototyping platform (before the Virtex-5 LX330 FPGA is mounted). The ZIF socket is convenient for the mounting and dismounting of the FPGA. 68*
- B.3 *(a) The LX330 FPGA is one of the largest FPGA in the Virtex-5 family. It contains 1200 user-configurable I/O’s, thus sufficient to control 1024 SLM pixels simultaneously. (b) The USB-JTAG programming cable connects the USB port of a computer to the JTAG port on the FPGA prototyping platform. The Xilinx ISE software programs the FPGA through this cable. 69*
- B.4 *Line driver circuit board, which amplifies the voltage amplitudes of 512 FPGA control signals from 3V to 16V. The circuit board contains two banana cable jacks, a Zener diode and a fuse for circuit protection, a bypass capacitor, connectors to connect from the FPGA circuit and to the SLM board, and 512 voltage-amplifying circuit made of bipolar transistors and resistors. 72*

- B.5 *Bipolar-junction-transistor (BJT) set up as a common-emitter amplifier for voltage amplification. Each 3V control signal from the FPGA circuit acts as the input to one common-emitter amplifier, and the output passes onto each SLM pixel after being amplified to 16V.* 73
- B.6 *Screen capture of the 4-layer line driver circuit board in the Allegro Cadence PCB design software, showing only the components and their padstacks, and board dimensions.* 74
- B.7 (a) *The SLM circuit board has a 34 mm × 34 mm square hole surrounded by 1040 gold bond fingers, designed to mount and to wire-bond the SLM chip. (b) Besides the SLM chip, the SLM circuit board also has 24 cable connectors which receives voltage-amplified control signals from the line driver circuit.* 75
- B.8 *Screen capture of the top layer of the 4-layer SLM circuit board in the Cadence PCB design software, showing partially the wire connections among the various components. The middle upper layer is the ground plane, while the middle lower layer is the power plane.* 76
- B.9 *Diagrams of SLM board showing how the SLM chip is mounted and wire-bonded onto the PCB (side-view (a) and top-view (b)).* 77
- B.10 *Detailed diagram near the square hole on the SLM board, with dimensions of the PCB bond fingers, and of the bond pads (schottky and ohmic contacts) of the SLM chip. Careful choices of the dimensions of bond pads and bond fingers, and the distances among them ensure successful wire-bonding.* 78
- B.11 *Microscope images of the wire-bonded SLM chip from VLSIP Technologies, Inc., showing the 1-mil gold wires between the die pads and the gold bond fingers on the SLM board before and after encapsulating the wires with Hysol[®] FP4450.* 79

Chapter 1

Introduction

The terahertz (THz) region of the electromagnetic spectrum lies in the gap between microwaves and infrared. This so-called 'terahertz gap' has historically been defined by the relative lack of convenient and inexpensive sources, detectors, and systems for terahertz waves. For frequencies below about 100 GHz (corresponding to a free-space wavelength of $\lambda = 3$ millimeters), electronic components can be purchased from a number of commercial suppliers, and millimeter-wave imaging systems are becoming available. Above 10 THz ($\lambda = 30$ microns), thermal (black-body) sources are increasingly efficient means for generating radiation, thermal cameras are commercially available, and optical techniques become more readily applicable. The two orders of magnitude of frequency spectrum in between are, relatively speaking, much less well explored (see Figure 1.1). Meanwhile, imaging with THz radiation offers many advantages such as submillimeter spatial and depth resolution, spectroscopic information, and unique material responses. Therefore, a wide range of terahertz imaging applications have emerged in the areas of aerospace, homeland security, medical imaging and quality control of packaged goods [1].

Terahertz imaging systems have become the subject of intensive research over the past 15 years. Yet, each of the existing implementations has its own disadvantages - speed, sensitivity, size, complexity, etc. One traditional method involves a raster-scan of the object to be imaged in front of the THz beam, while measuring and recording the transmitted (or reflected) THz wave at each scan position. This me-

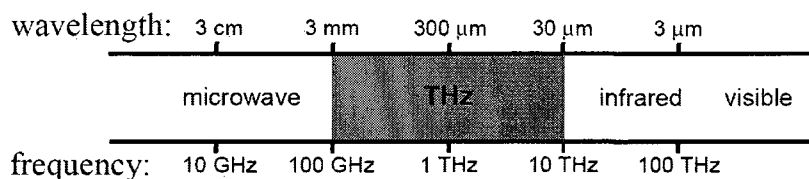


Figure 1.1 : *The terahertz region of the spectrum lies between microwaves and infrared, and is characterized by a free-space wavelength between 30 microns and 3 millimeters. The photon energy corresponding to $k_B T$ at room temperature, 40 meV, is equivalent to a frequency of about 10 THz.*

chanical scanning is slow; the acquisition time scales with resolution and the scan area. State-of-the-art technology takes around 6 minutes to scan a $100\text{mm} \times 100\text{mm}$ area at 0.25mm resolution [2]. Other approaches, such as that pioneered by researchers at MIT, involve the use of focal-plane techniques, similar to the pixel array inside a digital camera, to achieve real-time THz imaging [3]. However, these systems tend to have higher complexity and operational cost. For example, available array detectors, such as microbolometer arrays, are relatively insensitive to THz radiation, so a bright source is needed. Single-shot electro-optic sensing using crossed polarizers and a CCD camera also allows video-rate THz imaging [4], but this method requires a large and costly amplified femtosecond laser system. Yet, other recently developed imaging systems using more sophisticated image processing approaches, such as the Radon transform [5,6] and interferometric imaging [7], have shown preliminary successes but also face similar limitations in speed, resolution and/or hardware requirements. Clearly, novel imaging approaches are needed for improving the performance of terahertz imaging.

1.1 Terahertz imaging and compressive sensing

A newly developed theory in signal processing called compressive sensing (CS) has emerged in recent years. CS enables reconstruction of an image using many fewer measurements than are traditionally required [8,9]. The principle behind applying CS to the design of imaging systems is analogous to a two-step image encoding/decoding process: one can view image acquisition as the encoding step, and image reconstruction as the decoding step. For image acquisition, the goal is to efficiently capture the information about an object into a small set of measurements. For image reconstruction, CS relies on the common spatial structures present in real-world images. Based on the knowledge of these spatial structures, the CS reconstruction scheme “decode” the small set of measurements to recover a full image of the original object through an optimization procedure.

In general, when the number of measurements is significantly smaller than the total dimension of the image, the image reconstruction problem is undetermined, i.e., it has more than one solution. The CS encoding procedure (image acquisition) needs to ensure a one-to-one mapping between the class of images with certain spatial structure and the measurement space to allow exact image recovery. This thesis chooses two particular choices of encoding as the foundation to build CS THz imaging systems which acquires image fast, while keeping the hardware as simple as possible. The first CS Fourier THz imaging system acquires image data on the Fourier plane, and can reconstruct images with only a small subset of the complete 2-D Fourier transform data. Compared to traditional timed-domain raster scanning or uniform Fourier sampling on the full grid, partial sampling along a random path on the Fourier plane in this system can reduce the image acquisition time significantly. The second single-pixel CS imaging system performs compression simultaneously with image sampling

by modulating the THz beam with a set of random patterns. The system uses a weighted sum of all of the image pixels as each measurement, with weights of zero and 100% at random pixel locations [10]. This simple binary filtering can be easily implemented optically, by randomly blocking a subset of the pixels in the image and collecting the remaining light with a single lens.

Thanks to the CS theory, both systems already have benefits in imaging speed due to the reduced number of measurements required for reconstruction. The single-pixel CS imaging system, in principle, can achieve image acquisition at even higher speed if completely dispensed with all mechanical moving parts. However, the current technology has not yet developed a fast spatial light modulator (SLM) for THz beams to modulate the random patterns. Therefore, the second part of this thesis addresses the design and construction of high speed spatial terahertz modulators using active terahertz metamaterials [11,12]. After incorporating this device into the single-pixel CS imaging system, we no longer need to rely on mechanical moving parts as in traditional raster scanning systems. This system will still preserve the superior detection sensitivity of single-point detectors such as photoconductive antennas (rather than the lower sensitivity provided by existing multi-pixel arrays). As a result, we anticipate to achieve efficient terahertz imaging at a rate compatible with video imaging with simple, cost-effective hardware.

1.2 Scope of this thesis

Chapter 2 provides the background for the two major topics in this thesis, terahertz imaging and compressive sensing. Chapter 3 and 4 demonstrate the performance of the CS Fourier THz imaging system and the single-pixel CS THz imaging system respectively, through experimental results based on both imaging schemes. Chapter 5

describes the design and implementation of the first-generation THz SLM, and its capability, and the current development of the second-generation THz SLM with higher resolution and more pixels. Finally, chapter 6 poses the challenges remaining for the practical implementation of a future high-speed single-pixel THz imaging system.

Chapter 2

Background

2.1 Terahertz imaging

In the 1960's and early 1970's, the field of THz faced many challenges: a lack of suitable sources, sensitive detectors, and other components for the manipulation of radiation in this wavelength range. The development of terahertz imaging systems and techniques started in the 1990's after the invention of terahertz time-domain spectroscopy (THz-TDS), in which sub-picosecond optical pulses are used to generate broadband terahertz radiation, also via a second-order nonlinear optical process [13–15]. Hu and Nuss reported the first images acquired using THz-TDS (along with coining the term 'T-rays') in 1995 [16, 17]. These initial images (see Figure 2.1) inspired a great deal of excitement and much subsequent development of terahertz imaging systems and techniques. In the subsequent 15 years, the majority of research development in terahertz imaging are still based on THz-TDS. Therefore, let us first discuss this important THz system, its advantages and disadvantages, before going into the details of its application in THz imaging.

2.1.1 Time-domain terahertz system

The performance characteristics of a THz-TDS system has been reviewed in several previous publications [18–21], and will not be discussed in great detail here. Here provides a very brief description of the spectroscopic technique, and then focus on the

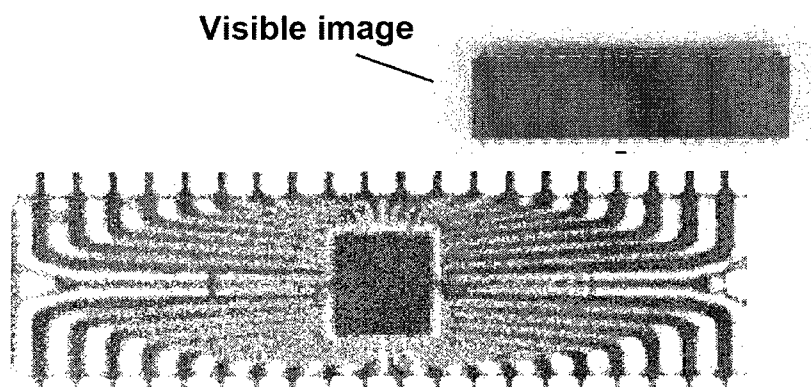


Figure 2.1 : *One of the first images acquired using a time-domain system, adapted from the original paper by Hu and Nuss. This shows a transmission image of a semiconductor integrated circuit, through the black epoxy package which is transparent to terahertz radiation. The metallization inside the package is clearly visible, as is the semiconductor wafer in the center. The spatial resolution of this image is roughly 250 microns. The inset shows an optical image of the sample.*

numerous features of this spectrometer which have proven advantageous for imaging.

A THz-TDS system starts with a femtosecond laser, producing a train of pulses of typically ~ 100 fs duration, at a repetition rate which is usually near 100 MHz. We split this pulse train into two using a beam splitter. One half is used to generate the terahertz radiation, by exciting a photoconductive antenna or by optical rectification, for example. The second half is used to gate a detector, typically either via a photoconductive or electro-optic interaction. Ideally the detector is sensitive to the incoming terahertz field only for a brief period of less than one picosecond. We can use this brief temporal window to sample the terahertz field at various delays, relative to the arrival of the terahertz pulse at the detection point. In other words, we determine the terahertz electric field as a function of time by measuring the value of $E_{THz}(t)$ at a particular value of t , and then repeat the measurement many times, at

many other values of t . To make these repeated measurements, we use many identical copies of the THz electric field. Sampling techniques of this sort, which rely critically on the precise synchronization between the terahertz field and the pulse used to gate the detector, are widely used in ultrafast optics and optoelectronics.

Optical sampling only works if every THz pulse in the pulse train is identical. If the shape of the THz pulse is evolving on a time scale comparable to (or shorter than) the measurement time, it is not possible to sample the waveform accurately. In addition to this fundamental issue, there are some other disadvantages to optical sampling. Like any sampling technique, it takes time to obtain the data. In principle, the acquisition time cannot be less than $N \cdot \delta t$, where N is the number of measured values of the electric field required in order to characterize the terahertz pulse, and δt is the pulse-to-pulse spacing of the pulse train. Because we usually take advantage of signal averaging, the acquisition time is usually much longer than this minimum value. Another problem inherent to sampling measurements is that they require a method for varying the delay of the sampling gate (i.e. the probe pulse) relative to the terahertz pulse. This is most often accomplished using a mechanical delay line, moving a mirror to vary an optical path length.

It is important to note that, using either photoconductive sampling [14, 22] or free-space electro-optic sampling [23–25], one obtains a direct measurement of the terahertz electric field $E(t)$, not merely intensity $I(t)$. In both cases, the measurement is sensitive only to coherent radiation, and moreover only to radiation which is phase-locked to the repetition rate of the femtosecond oscillator. As a result, both of these sampling techniques are blind to thermal radiation, and therefore the detection operates at room temperature without degradation of performance. This eliminates the requirement for liquid cryogenics which had previously limited the broader use of

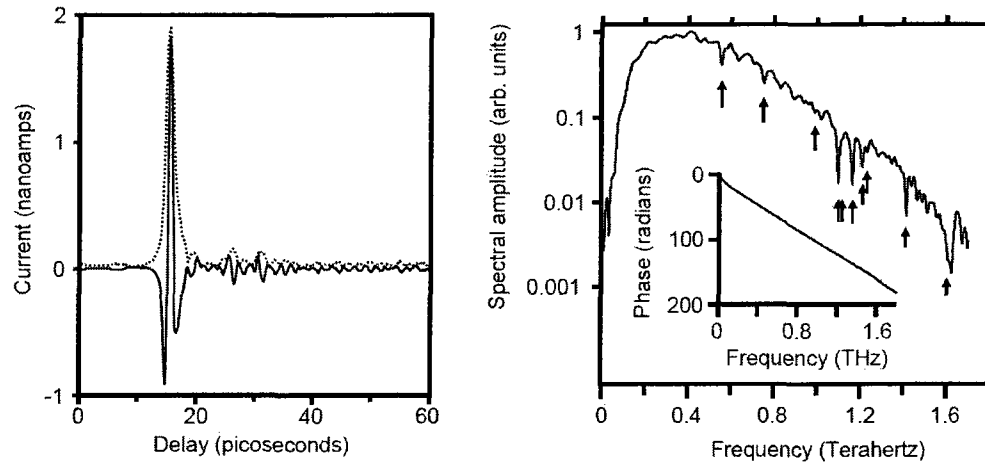


Figure 2.2 : (left) A typical time-domain terahertz waveform, measured in ambient air. The oscillatory features which follow the initial single-cycle transient are the result of water vapor in the beam path. The dotted curve shows the intensity envelope, computed from the measured electric field $E(t)$ using a Hilbert transform. (right) The spectral amplitude $|E(\omega)|$ derived from the field shown at left by Fourier transform, on a log scale. The vertical arrows indicate the spectral positions of tabulated water vapor absorption lines. The inset shows the spectral phase, also derived from the time-domain measurement. This is essentially linear, as expected for a single-cycle pulse. The effects of the water vapor absorption lines on the phase are measurable, but are too small to see in this display.

THz spectrometers.

Other useful aspects of the time-domain spectrometer are illustrated by Figure 2.2, which shows a typical waveform and the corresponding spectral amplitude and phase. The left panel shows the raw data from a photoconductive sampling measurement, which is the photo-induced current in a terahertz substrate antenna as a function of the delay between the terahertz pulse and the optical gate pulse. This is approximately proportional to the terahertz electric field $E(t)$, which contains both amplitude and phase (i.e., timing) information.

Another unique characteristic of THz-TDS is the broad bandwidth of the radiation, broader than any other source (other than a thermal source) in the terahertz range. Typically, the bandwidth can span more than an order of magnitude in wavelength. Broadband coverage is valuable for spectroscopic measurements, which can be used to identify the chemical composition of unknown materials in an image or to locate materials according to their terahertz absorption signatures.

It is also worth noting some of the limitations of working with THz-TDS systems. A primary difficulty is the power in the THz beam, which is quite low (typically less than $1 \mu\text{W}$ average power) because of the inefficiency of non-linear optical mixing. However, the dynamic range can be quite high in THz-TDS, even though the THz power is low [26]. This is a result of the coherent detection which effectively rejects many common sources of noise. This high dynamic range permits measurements even in situations where only a tiny fraction of the generated radiation reaches the detector. Nevertheless, it is important to note that existing commercially available focal plane detectors (such as, for example, pyroelectric cameras) require much more power to operate than the THz-TDS systems generally produce (e.g., a minimum power level of $100 \mu\text{W}$ per illuminated pixel). As a result, the majority of time-domain imaging systems rely on raster scanning of either the THz beam or the object, so that images can be assembled serially using a single detector or perhaps a few operating in parallel. *This places a significant limitation on the image acquisition rate. Concerns about power may also play a role in experiments which require long distance atmospheric propagation or which seek to study material nonlinearities at terahertz frequencies.*

Other difficulties are inherent in the nature of the time-domain system. For instance, the time-domain scanning puts a practical upper limit on the spectral resolution which can be achieved. The spectral resolution δf is given by the inverse of the

duration of the temporal scan, which in most cases is limited by the length of a scanning delay line as in a conventional Fourier transform spectrometer. With 15 cm of travel, a typical mechanical delay line will provide up to 1 nanosecond of delay range, corresponding to $f = 1$ GHz. This value is inadequate for high-resolution applications such as gas-phase spectroscopy [18]. Also, experiments which require radiation in the higher frequency range may require a source other than THz-TDS. The high dynamic range typically quoted for THz-TDS measurements is a frequency-dependent quantity, which decreases exponentially with increasing frequency as shown in Figure 2.2 [27]. Thus, a THz-TDS system may compare very favorably to an electronic cw system based on a Gunn diode operating below 1 THz, for example [25], but would perform less well in comparison to a quantum cascade laser operating at 4.9 THz [3]. Finally, one practical disadvantage is the requirement for a femtosecond optical source. Recent dramatic advances in femtosecond fiber laser technology are beginning to overcome this problem, but the laser is still the most expensive and sophisticated piece of equipment in the spectrometer.

2.1.2 Imaging with a time-domain spectrometer

The first TDS imaging system, reported in 1995, implemented an operational method which has subsequently been replicated many times [16, 17]. A typical system diagram is shown in Figure 2.3. This shows a time-domain spectrometer based on photoconductive antennas electro-optic generation and detection are also commonly used [28, 29]. In order to be suitable for image formation, a second set of focusing optics are inserted into the THz beam to form an intermediate focal spot halfway between the THz transmitter and THz detector.

For image acquisition, one of the key considerations is the rate at which THz

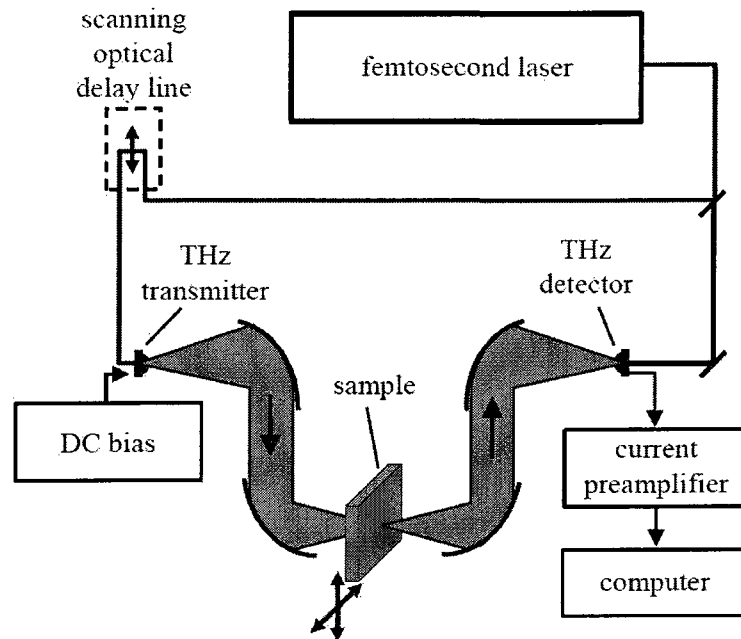


Figure 2.3 : A schematic of a typical transmission-mode raster-scan time-domain imaging system.

waveforms can be acquired, since this often determines the time for forming an image. Typically, a motorized scanning stage is used to raster the object to be imaged through the terahertz beam focus, so that image data is acquired one pixel at a time. In the earliest example, THz waveforms were measured at a rate of 20 waveforms per second, so acquiring a 100×100 pixel image took close to 10 min. This rate was determined by the scan rate of the optical delay line, a galvanometric scanner with a corner cube mirror. Modern THz imaging systems which use this raster-scanning method employ more sophisticated methods for generating optical delay, and thus can run at substantially higher speeds. In such systems, however, there is frequently a trade-off between the scan range (as measured in picoseconds) and the scan rate (number of

waveforms per second). The highest scan rates (e.g. thousands of waveforms per second) can be achieved using a piezo-electric device, but with a limited (tens of picosecond) scan range. At these higher rates, the image acquisition time may no longer be limited by the time to measure a THz waveform, but instead by the rate at which the object (or the THz beam) can be raster scanned. However, the more limited scan range does limit the information contained in each waveform. As noted above, a shorter scan range limits the spectral resolution of the measurement. A shorter scan range also limits the range of depths to which the THz pulse can penetrate through a material and still be detected, since a larger optical depth could delay the pulse outside of the temporal window of the measurement. This latter effect will be illustrated more clearly in the discussion of time-of-flight imaging (see below). Other types of mechanical scanning devices (e.g. spinning mirror devices) can generate several hundreds of picoseconds of delay range with a scan rate in the vicinity of 100 Hz [30]. In any event, the motion of the scanning delay line must be synchronized to the raster scan of the object, so that it is possible to determine the location of the object at the moment each waveform is acquired.

Recently, several groups have demonstrated that it is possible to dispense with the mechanical scanning delay line entirely, and instead make use of asynchronous optical sampling [31, 32]. In this approach, two femtosecond lasers are used instead of one. The repetition rate of one laser is locked to that of the other, with a fixed frequency offset. One laser is used to generate the THz pulse, and the second to gate the detector. In this way, the delay of the THz pulse sweeps automatically, relative to the gating of the detector, at a rate which is determined by the frequency offset between the two lasers. This eliminates the moving parts, at the expense of a second laser and feedback electronics.

Once the data are acquired, the next task is the formation of an image. A full data set consists of a complete THz time-domain waveform (see Figure 2.2) corresponding to each pixel of the image. These waveforms obviously contain a great deal of information: the amplitude and phase of the transmitted terahertz pulse, for many spectral components. A two-dimensional false-color image can be formed using any subset of this large data set. Typically, images formed using different portions of the data contain different types of information about the sample. For example, peak-to-peak amplitude of the THz time-domain pulse conveys the amount of THz absorption at different parts of the imaged object, whereas spectral phase and time delay of the transmitted THz pulse encode the thickness of the imaged object.

2.1.3 Other imaging methods

Most imaging techniques using THz-TDS relies on a raster-scanning method, to acquire image data pixel by pixel. Other more sophisticated approaches which are not discussed here, such as THz tomography and interferometric imaging [5–7], also face similar speed limitations. This can be a limiting factor in some applications, since serial acquisition of image data can be quite slow. One solution would be the development of a sensitive focal plane array detector, an area of active research [33]. Ultrafast optics offers another solution to this problem, using the free-space electro-optic sensing technique described above. Among the two, we will first discuss the latter.

As noted, electro-optic sampling relies on an induced polarization rotation in a femtosecond probe pulse, which depends on the amplitude and direction of the terahertz field. Because the detected signal is an optical one (i.e. polarization rotation of an optical probe beam) rather than an electrical one (photo-induced current in a

metal antenna), the sampled region is defined by the size of the optical probe and of the non-linear crystal rather than by the size of an antenna. So, instead of using a small electro-optic crystal and a focused THz beam, one can use a large (cm^2) crystal and a large-area beam. The spatially varying polarization rotation of the probe beam can be measured using crossed polarizers and a CCD camera [29]. Since a CCD detector array can refresh at video rates, this technique can be used to generate terahertz movies [4, 34, 35]. It does, however, require considerably more optical power in the femtosecond probe beam. Generally, an amplified femtosecond laser system is required. Also, one still requires a mechanical delay line to vary the delay between the probe pulse and the THz pulse in order to obtain a measurement of the terahertz electric field.

X.-C. Zhang and co-workers have also developed a chirped-pulse technique for measuring an entire THz waveform along a line (1D imaging) in a single shot, entirely dispense of the delay line [36–38]. However, this system has a limited temporal resolution, and also requires an amplifier which increases the cost and complexity of the laser system. The only electro-optic imaging system which does not require an amplified laser source uses a time-of-flight camera comprising an optical demodulation detector array [39].

In parallel with the rapid progress in pulsed time-domain techniques, tremendous strides have also been made in technologies for continuous wave (cw) terahertz systems since the first examples [40, 41]. With some exceptions [42–44], cw THz imaging systems typically employ an incoherent device for direct detection of the THz wave, such as a bolometer or a Golay cell. Array detectors are also available for direct (not heterodyne) detection, including microbolometer arrays [33, 34], germanium detector arrays [45], and pyroelectric cameras. Unlike in the case of THz-TDS, the source and

detector are independent devices, rather than two components of a coupled system. In some cases, the terahertz source is tunable, in which case it is possible to combine spectroscopic measurements with imaging just as in the time-domain systems.

One important advantage of imaging with a single-frequency source is the ability to select the source wavelength to optimize the imaging capability. This is relevant, for example, in the case of imaging at a stand-off distance. Stand-off imaging (i.e. at greater than a few metres distance) is challenging because of the presence of atmospheric water vapour, which significantly attenuates the terahertz beam. However, at certain frequencies within the terahertz range, the atmospheric attenuation is minimized because there are no nearby strong water vapour absorption lines. The ability to tune the terahertz source to a water 'window' is a considerable advantage. For example, for a 25m stand-off, the power throughput from transmitter to receiver increases by more than a factor of 10 if the atmospheric loss decreases by only 0.5 dB m^{-1} . For comparison, variations of several dB m^{-1} can be achieved by frequency tuning within narrow windows in the 4-5 THz range. Real-time imaging at a 25m stand-off has been demonstrated using a terahertz quantum cascade laser (QCL) and a room-temperature microbolometer array [33, 46]. In this demonstration, the QCL was held at 30 K, within the range of a thermomechanical cooler that does not require liquid cryogenics, and produced $\sim 17\text{mW}$ of power in pulsed operation. A few per cent of the emitted power reached the imaging array, sufficient for imaging with a 1 s integration time. Future THz imaging systems with cw sources mainly rely on the development of QCL at room temperature [47], and detector arrays with higher sensitivity in the THz range.

2.1.4 Terahertz imaging applications

The idea of using terahertz radiation for imaging and sensing, in analogy to the many similar applications of both optical and microwave radiation, has been discussed for at least several decades. Early researchers speculated on the use of sub-millimeter waves for seeing through fog or haze with reduced scattering losses, locating objects hidden in camouflage, and detecting defects in optically opaque materials, in addition to other research areas such as high bandwidth communications and metrology. More recently, this list of promising applications has grown to include security screening such as weapon detection [48, 49], quality control such as accurate measurement of paint thickness [50], non-destructive testing such as detection of defects inside spacecraft foam insulation [51], and spectroscopic characterization of materials such as illicit drug detection [52]. Many of these ideas exploit the unique properties of terahertz radiation which include the transparency of common packaging materials such as cardboard and plastics, the submillimeter wavelength which permits imaging with a diffraction-limited resolution similar to that of the human eye, and the fact that many interesting materials exhibit unique spectral fingerprints in the terahertz range which can be used for identification and chemical analysis. Due to its non-invasive nature, THz imaging research have also expanded into the fields of medical diagnosis [53] and the study of historical art such as mural paintings [54].

2.2 Compressive sensing (CS)

2.2.1 CS background

Traditionally, digital signal processing involves first uniformly sampling a signal and then processing it in some way that enhances it and/or prepares it for storage or

transmission. One such example is THz imaging based on raster scanning. The raster-scan imaging system obtains each image sample by measuring the THz transmission/reflection at each spatial position of an object on a uniform grid. This kind of uniform sampling is governed by the signal's Nyquist rate. The sampling rate must be twice the bandwidth in order to accurately represent the signal/image.

There are many scenarios in which a signal may have a large bandwidth, but does not contain a lot of information. For instance, a piecewise smooth signal may have high frequency components necessitating many samples, but can be represented well by a linear combination of only a few wavelets. In digital photography an image field may be sampled at 10 million locations, but this information can be effectively stored with only 100 thousand DCT or wavelet coefficients. *Compressive sensing* (CS) takes the logical step of exploiting a signal's structure to acquire it in fewer measurements, rather than the observe the whole thing and compress it later. As a model for structured signals, we first consider compressible signals that are k -sparse in some orthogonal basis Ψ . This means that when represented in the basis, the signal has only k non-zero coefficients, where k is much smaller than the signal length N . Let us now consider an image (or a 2-D signal; this discussion will use the terms, "signal" and "image" interchangeably). Consider the object a length- N signal x of dimension indexed as $x(n)$, $n \in \{1, 2, \dots, N\}$. In this case, x is a 2-D image with pixels ordered in a $N \times 1$ vector. The image can also be represented in terms of the coefficients $\{\theta_i\}$ of an orthonormal basis expansion $x = \sum_{i=1}^N \theta_i \psi_i$ where $\{\psi_i\}_{i=1}^N$ are the $N \times 1$ basis vectors. Forming the coefficient vector α and the $N \times N$ basis matrix $\Psi := [\psi_1 | \psi_2 | \dots | \psi_N]$ by stacking the vectors $\{\psi_i\}$ as columns, we can write the samples as $x = \Psi\theta$. The image x can be k -sparse, meaning that the coefficient vector θ is sparse, where only $k \ll N$ coefficients are non-zero. Or x can be r -compressible, meaning that the sorted

coefficient magnitudes decay under a power law with scaling exponent $-r$. We are interested in recovering these signals exactly, with as few measurements as possible.

The first half of CS is the definition of a special linear, nonadaptive measurement scheme. For a given k -sparse signal $x \in \mathbb{R}^N$, the measurements can be represented mathematically as

$$y = \Phi x = \Phi \Psi \theta. \quad (2.1)$$

The matrix Φ is of size $M \times N$, with $M < N$. The measurement process is nonadaptive in that Φ does not depend in any way on the signal x . We would like the matrix Φ to have the property that no two k -sparse signals can result in having the same measurements y . Mathematically speaking, Φ must be an injective mapping for k -sparse signals. It has been shown that with high probability, random matrices of i.i.d Gaussian (white noise) or ± 1 entries (from a uniform Bernoulli distribution) satisfy this property for sufficiently large M [8, 9]. Other possible choices include randomly permuted vectors from standard orthonormal bases, or random subsets of basis vectors, such as Fourier or Walsh-Hadamard bases.

The second half of CS is recovering a signal \hat{x} from the measurements $y = \Phi x$. This is an ill-posed problem, since an infinite number of potential solutions all will admit the given measurements. However we will choose as \hat{x} the one that has the sparsest representation. To find this we perform the optimization

$$\hat{x} = \arg \min_x \|x\|_0 \text{ s.t. } y = \Phi x. \quad (2.2)$$

This optimization of the ℓ_0 pseudo-norm ($\|x\|_0$ is the number of non-zero elements of x) finds, among all signals that satisfy the linear measurements, the signal that has the fewest number of non-zero elements. Such an optimization is combinatorial and

therefore impractical. Instead, we consider the optimization

$$\hat{x} = \arg \min_x \|x\|_1 \text{ s.t. } y = \Phi x, \quad (2.3)$$

where the ℓ_1 norm of a signal is defined as the sum of the absolute values of its components:

$$\|x\|_1 = \sum_i |x_i|. \quad (2.4)$$

When the signal x is sparse in another reconstruction basis Ψ (such as wavelets), the reconstruction algorithm substitutes $x = \Psi\theta$ in the constraint in equation (2.3) and solve for the minimum l_1 -norm of θ instead. Equation (2.3) is a convex optimization that can be formulated as a linear program known as *basis pursuit* [55]. There also exists a range of alternative reconstruction techniques based on greedy, stochastic, and variational algorithms [56]. The major ones used in this thesis are the SPGL1 algorithm [57] and the minimization of total variation (min-TV) [9,58]. The attractive property of CS Φ matrices is that this polynomial-time optimization procedure, under the CS measurement scheme, yields perfect recovery of k -sparse signals when Φ takes $O(k \log(N/k))$ measurements.

If x is not sparse, but can be represented well by its k largest components in some basis, then the error of the reconstructed signal \hat{x} is only a constant times the error between x and its k -term approximation. Or if the measurements y are corrupted by noise, then the solution to the alternative ℓ_1 minimization, known as *basis pursuit with inequality constraints* (BPIC) [59]

$$\hat{x} = \arg \min_x \|x\|_1 \text{ s.t. } \|y - \Phi x\|_2 < \epsilon, \quad (2.5)$$

satisfies $\|\hat{x} - x\|_2 < C_N \epsilon + C_k \sigma_k(x)$ with overwhelming probability. C_N and C_k are the noise and approximation error amplification constants, respectively; ϵ is an upper

bound on the noise magnitude, and $\sigma(x)$ is the ℓ_2 error incurred by approximating x using its largest k terms. This optimization can be solved using standard convex programming algorithms.

For a more thorough review of CS and its application to imaging, see the article by Duarte *et al.* [10].

2.2.2 CS imaging applications

Major applications of CS to imaging have included tomography [9], the optical single-pixel camera [10,60], hyper-spectral imaging [61], digital holography [62], geophysical imaging [63,64], and medical imaging such as magnetic resonance imaging (MRI) [65] and photo-acoustic imaging [66].

In its wide range of applications to imaging, the CS theory has inspired new imaging system designs which feature simpler hardware, and/or acquisition schemes which feature better imaging efficiency. For instance, applying CS to MRI improves the spatial resolution of MRI images limited by MRI scanning hardware, and allows better image reconstruction from reduced sampling, thus accelerating acquisition for patient comfort [65]. Both the optical single-pixel camera [10,60] and the single-pixel THz imaging system in Chapter 4 use a single-pixel detector instead of a conventional CCD array for imaging in visible light. In both cases, CS enables the implementation of an imaging system with simpler and less expensive hardware, i.e., the single-pixel detector.

Chapter 3

A CS Fourier terahertz imaging system

This chapter describes the first example of compressive sensing (CS) applied to THz imaging. We demonstrate successful reconstruction of a target's image with a randomly chosen subset of the samples from the Fourier plane. We also combine CS with traditional phase retrieval (PR) algorithms [67] for image reconstruction with only a random subset of the Fourier amplitude image. Incorporation of CS into THz imaging system designs can significantly reduce the image acquisition time.

3.1 Imaging setup

Our imaging system consists of a pulsed THz transmitter and receiver, both based on photoconductive antennas, and two lenses, one of which approximately collimates the THz beam while the other focuses the beam (see Figure 3.1). The object mask, placed in between the two lenses, scatters the THz waves. The focusing lens forms the Fourier transform of the object mask at its focal plane. The receiver, mounted on a translation stage, performs a raster scan in the focal plane, over an area of 64×64 mm, at 1 mm intervals. A circular aperture (1 mm in diameter) is placed in front of the receiver antenna so that it only samples a small area of the Fourier pattern, rather than relying on the ~ 6 mm receiver aperture [68]. The object mask is made of opaque copper tape on a transparent plastic plate. The object mask used in the experiments in this chapter is an R-shaped hole, 34mm by height and 31mm by width.

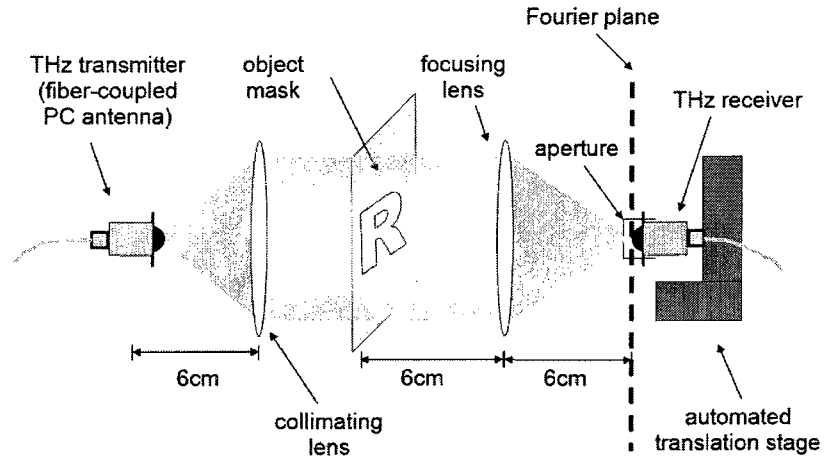


Figure 3.1 : *The THz Fourier imaging setup. An approximately collimated beam from the THz transmitter illuminates an object mask, placed one focal length away from the focusing lens. The THz receiver raster-scans and samples the Fourier transform of the object on the focal plane.*

3.2 Experimental results

During raster-scanning of the detector in Figure 3.1, an entire time-domain THz waveform is measured at each detector position. The reconstruction algorithm first computes the power spectrum of each waveform, selects the spectral amplitude and phase at a particular wavelength ($\lambda = 1.5$ mm) to obtain a (complex) pixel value, and assembles a 64×64 Fourier image. The following sections demonstrates various schemes to reconstruct an image of the object from this Fourier data.

3.2.1 Fourier reconstruction with full dataset

Direct 2D Fourier inversion of this image reconstructs the object mask as shown in Figure 3.2(a). The pixel size is given by $\Delta x = \frac{\lambda f}{X}$, where X is the length in one dimension of the raster scan area (64 mm) and f is the focal length of the focusing

lens (60 mm). Thus we obtain a pixel size of $\Delta x = 1.406$ mm in both dimensions, at the chosen wavelength.

In order to estimate the resolution of the reconstructed image in Figure 3.2(a), a 5×15 region containing the left “leg” of the “R” is selected. After averaging the 5 selected rows, the resulting trace can be approximated by the convolution of a rectangular function with a Gaussian function with unknown variance (σ^2). The width of the left “leg” of the “R”, i.e., the width of the rectangular function, is 8mm (measured by a ruler). One can then estimate σ^2 of the Gaussian function to fit the average trace. The estimate for σ^2 is around 1mm^2 , equivalent to a Full-Width Half-Maximum (FWHM) of 2.354mm or 1.68 pixels, which is defined as the resolution of our reconstructed image. This 2D Fourier inversion technique requires measurements at all 4096 pixel locations, and is therefore slow.

3.2.2 CS reconstruction with partial dataset

Image reconstruction using CS can achieve good image reconstruction quality from only a small randomly chosen subset of these 4096 pixels, thus speeding up the imaging process. Consider the object mask a length- N signal x of dimension indexed as $x(n)$, $n \in \{1, 2, \dots, N\}$. In this case, x is a 2D image with pixels ordered in a $N \times 1$ vector, where $N = 4096$. View the Fourier measurements as projections, $y(m) = \langle x, \phi_m^T \rangle$, of the signal x onto a set of Fourier basis functions $\{\phi_m\}$, $m \in \{1, 2, \dots, M\}$ where ϕ_m^T denotes the transpose of ϕ_m and $\langle \cdot, \cdot \rangle$ denotes the inner product. Direct 2D Fourier inversion requires the full dataset, $M = N = 4096$ measurements for image reconstruction. However, CS uses only a much smaller number of measurements than the number of pixels in the image, i.e., $M < N$. In matrix notation, the CS system measures $y = \Phi x$, where y is an $M \times 1$ column vector of measurements

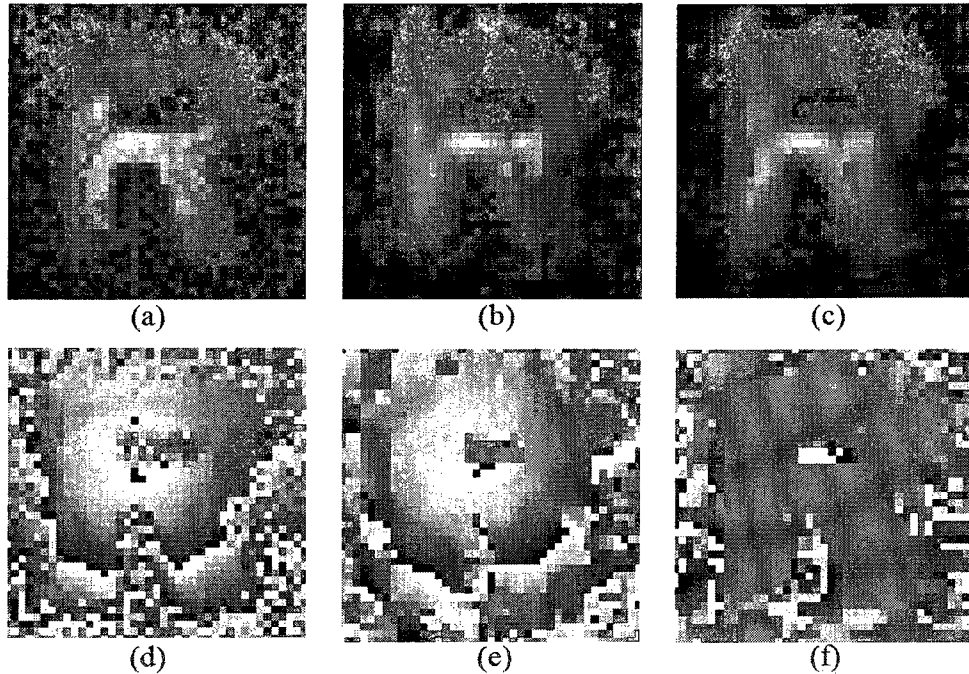


Figure 3.2 : *Compressed sensing imaging results. (a) Magnitude of image reconstructed by inverse Fourier transform using the full data set (4096 uniformly sampled measurements), and (d) its phase. Note the phase distortion inherent in the THz beam in (d). Compressed sensing reconstruction result using 500 measurements (12%) from the full data set: (b) magnitude, and (e) phase. Compressed sensing with phase correction improves image quality and eliminates phase distortion (see (c) and (f)). All figures show a zoom-in view on a 40×40 grid centered on the object.*

and the measurement matrix Φ is $M \times N$. Despite using fewer measurements, CS can achieve perfect reconstruction of the object, assuming its sparsity, through an optimization procedure [8]. Many optimization algorithms exist to solve this inverse imaging problem. These algorithms aim to solve the minimization problem:

$$\operatorname{argmin} \|x\|_1 \text{ subject to constraint } y = \Phi x, \quad (3.1)$$

where $\|x\|_1$ denotes the l_1 -norm [8]. Sometimes, when the original image x is

sparse in another reconstruction basis Ψ (such as wavelets), the reconstruction algorithm substitutes $x = \Psi\theta$ in the constraint in equation (3.1) and solve for the minimum l_1 -norm of θ instead. Figure 3.2(b) demonstrates the CS reconstruction result using only 500 measurements out of the total 4096 measurements through the SPGL1 algorithm described by van den Berg *et al* [57]. Using CS allows a reduction of the number of measurements required for image formation by more than a factor of eight.

We desire to further improve the reconstruction result by removing the background profile of the phase, which is not due to the object but is inherent in the spherical wavefront curvature of the Gaussian beam illumination of the object (see Figure 3.2(d)). As a result, the phase in the Fourier plane is distorted by the superposition of a spherically varying background. We first remove the object mask in the setup and obtain a 64×64 image of the background phase of the beam through 2D Fourier inversion. These phase values at each pixel form the diagonal entries of a matrix P . Similar to the modification suggested by Lustig *et al* [65], we insert this diagonal matrix P after Φ in equation (2.3) and then solve the phase-corrected optimization problem for image reconstruction. This phase correction procedure not only removes the spherically varying phase profile in the reconstruction (compare Figure 3.2(f) to (d-e)), but also improves the quality of the reconstruction (compare Figure 3.2(c) to (b)). Using the same procedure as for Figure 3.2(a) to estimate the reconstructed image resolution, we obtain a resolution of 4.19 pixels and 3.35 pixels for Figure 3.2(b) and (c) respectively.

Figure 3.3 plots the mean-square error (MSE) between the magnitudes of the reconstructed image and the reference image in Figure 3.2(a), normalized by the energy of the reference image, against the number of measurements used in CS. Since

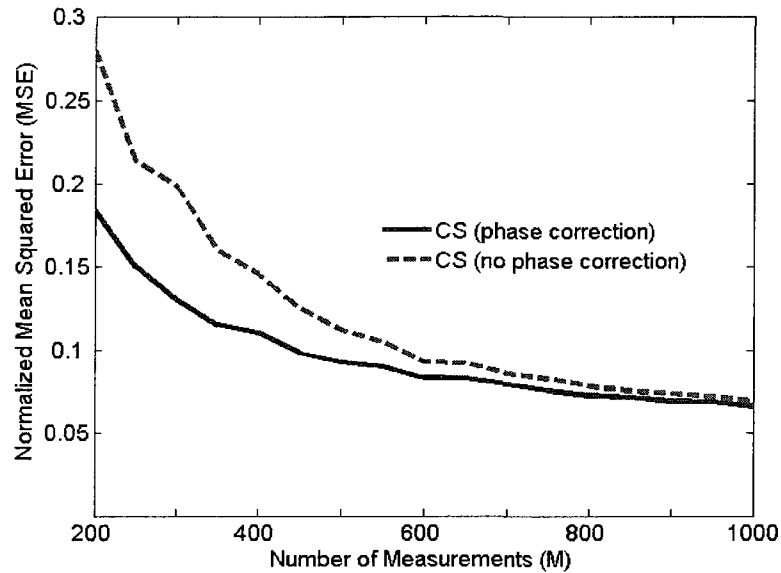


Figure 3.3 : Comparison of quality of image reconstruction between CS with and without phase correction. As the number of measurements (M) used in CS increases, the mean-squared error (MSE) between the magnitudes of the reconstructed image and the reference image (see Fig 3.2(a)), normalized by the energy of the reference image, decreases. CS with phase correction shows superior reconstruction performance.

an object with a constant phase profile has a more sparse representation in wavelet basis than one with a spatially varying phase profile, CS reconstruction using phase correction yields superior performance for a given number of measurements.

3.2.3 CS and phase retrieval

If the object mask in Figure 3.1 moves away from the object plane, the acquired Fourier data will have the correct Fourier magnitude but a distorted phase. No longer can one use the phase data for image reconstruction. However, an image can still be reconstructed by combining CS with the well-known technique of phase retrieval (PR) [67]. Moravec *et al.* recently developed a PR minimization algorithm, called

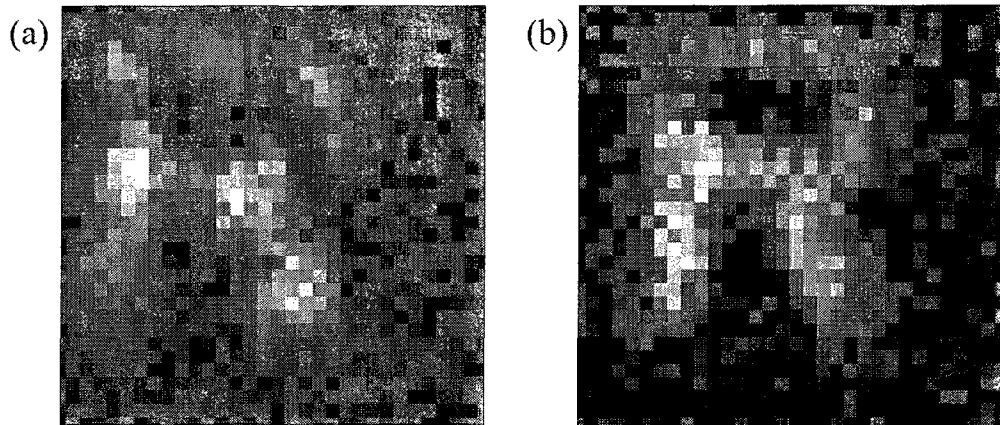


Figure 3.4 : *Image reconstruction results using (a) compressive phase retrieval (CPR) with the full data set (4096 magnitude measurements), and (b) compressed sensing phase retrieval (CSPR) with a subset of 1500 measurements from the data set used in (a).*

compressive phase retrieval (CPR), which uses the full Fourier amplitude dataset [69]. The same paper also describes a compressive sensing phase retrieval (CSPR) algorithm which enables reconstruction with a subset of the Fourier amplitude samples. It is particularly challenging for PR to reconstruct complex-valued images of objects with a nonuniform phase profile. Therefore, we modify the original Fourier dataset such that, when applying the CPR and CSPR algorithms, we assume that the illuminating beam is a perfect plane wave. We first obtain the inverse Fourier image of the object (magnitudes and phases) as in Figure 3.2(a) and (d) from the 4096 measurements. Then, we keep the magnitude of this spatial image unaltered but remove its phase using the background phase profile of the beam. The magnitude of the Fourier transform of this phase-corrected spatial image is the input to our CPR and CSPR algorithms. Figure 3.4(a) and (b) show the reconstruction results from CPR with the full dataset and from CSPR with 1500 measurements respectively.

3.3 Discussion

The THz Fourier imaging scheme in this chapter could be useful for quality control applications, such as detection of point impurities in manufactured products, because Fourier-domain measurements are particularly sensitive to sharp point-like features.

The CSPR reconstruction results demonstrate the applicability of our imaging scheme not only to pulsed THz imaging systems but also to continuous-wave systems, in which phase information is typically not available. The latest research on THz CW imaging requires high-power sources (>10 mW), such as quantum-cascade lasers (QCLs) operating at low temperature (~ 30 K), because the focal-plane microbolometer array used for imaging has low sensitivity at THz frequencies [3]. In contrast, the Fourier imaging technique with CSPR can use a single-pixel THz detector with much higher sensitivity to enable imaging with a low-power CW source.

In both the CS and CSPR examples in this chapter, the reduction of measurements enabled by compressive sensing can significantly reduce the image acquisition time. Traditional THz imaging systems scan point by point in the space domain. By application of the CSPR theorem, only $O(k^2 \log(4N^2/k^2))$ locations in the frequency (modulus) domain need to be scanned if the signal is sparse in space and has k nonzero values. Because a scanner must stop at every location to make a measurement, taking fewer measurements will result in less scan time. In addition, the scanner does not have to travel as far, either. The path length traveled by a scanner to k^2 random points on an $N \times N$ square lattice is, on average, $.93kN$ [70]. For $k \ll N$, this is a significant improvement over the N^2 distance required for a full raster scan. Assuming a 0.1 m/s constant scanning speed of the receiver with no signal averaging, a full raster scan takes around 41 seconds. Scanning a random subset of 500 measurements requires only 13 seconds, i.e., a $2/3$ reduction of the total acquisition time.

Despite its reduction in image acquisition time compared to existing imaging systems, the CS THz Fourier imaging scheme still relies on mechanical scanning. The mechanical moving parts in the system are major limitations to high-speed imaging. Future THz imaging systems should require more sophisticated technology, in both hardware and software, to speed up the acquisition, while maintaining sufficient image resolution. The single-pixel imaging approach in Chapter 4 will take us one step closer to meet this goal.

Chapter 4

A Single-pixel CS terahertz imaging system

Most existing THz imaging systems, including the CS Fourier imaging system in Chapter 3, use a raster-scan to move an object in front of a single pixel detector. This mechanical scanning significantly limits the acquisition speed [2,48,51,52]. With state-of-the-art technology, it takes about 6 minutes to scan a $100\text{mm} \times 100\text{mm}$ area at 0.25mm resolution [2]. Real-time THz imaging has been demonstrated using focal-plane detector arrays [3,4]. However, these systems tend to have higher complexity and operational cost. For example, available array detectors, such as microbolometer arrays, are relatively insensitive to THz radiation, so a bright THz source is needed [3]. Single-shot electro-optic sensing also allows video-rate THz imaging [4], but this method requires a large and costly amplified femtosecond laser system. One implementation of the electro-optic imaging system can use a non-amplified laser source [39], but, just like other typical pulsed THz systems, this system will not have enough source power to image objects with high THz attenuation or at a long distance. Even though interferometric or tomographic approaches have significantly reduced the number of required measurements by, for example, non-uniform sampling in the Fourier domain, the acquisition speed of such systems are still limited by raster scanning unless a full detector array is used [5–7]. THz reciprocal imaging can achieve high-speed imaging with a single-pixel detector but requires an unconventional source array, with each source element modulated at a different frequency [71].

For practical, time-critical applications, a THz imaging system should not require

raster scanning of the object or the THz beam. In addition, one would like to preserve the superior detection sensitivity of a single-point detector such as photoconductive antennas (rather than the lower sensitivity provided by existing multi-pixel arrays) and the simplicity and spatial coherence of a point-source transmitter. This chapter describes a single-pixel THz imaging system based on an advanced signal processing theory called compressed sensing (CS) [8, 9], which enables both of these objectives. In contrast to the THz Fourier imaging setup using CS and phase retrieval described in Chapter 3, this system does not require mechanical scanning of the THz receiver on the image plane.

The rationale behind the improved acquisition speed of the single-pixel terahertz camera is twofold. First, this camera performs compression simultaneously with image sampling by modulating the spatial profile of the THz beam with a set of random patterns, a technique enabled by CS. This imaging scheme requires significantly fewer samples than the total number of image pixels to fully reconstruct an image, thus speeding up the acquisition process [8, 9]. Second, the speed of most existing THz imaging systems is limited by the need to mechanically raster-scan the object (or the THz beam) [1]. The method described in this chapter replaces this mechanical scanning with the spatial modulation of the free-space THz beam, which can in principle be much faster.

4.1 CS imaging principle

The principle behind the design of CS imaging systems can be summarized in the equation $y = \Phi x$, where y is an $M \times 1$ column vector of measurements, x is an image with N^2 pixels ordered in a $N^2 \times 1$ vector and the measurement matrix Φ is $M \times N^2$. Using CS, we acquire a much smaller number of measurements than the number of

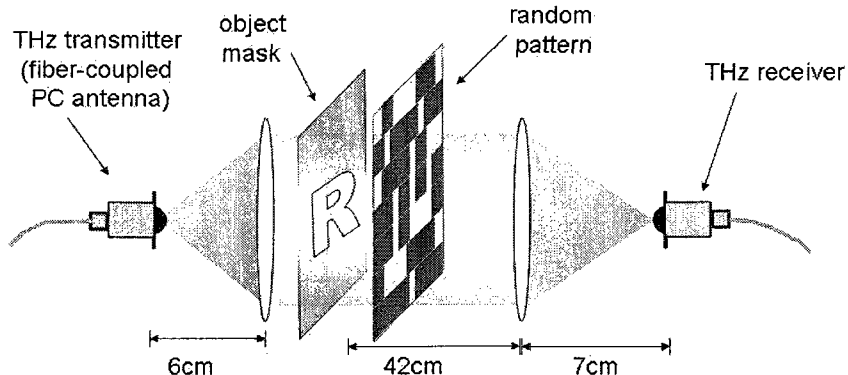


Figure 4.1 : *The THz compressive imaging setup. An approximately collimated beam from the THz transmitter illuminates an object mask and is partially ($\sim 50\%$) transmitted through a random pattern of opaque pixels. The random patterns, the focusing lens and the receiver are placed in order to most efficiently focus the THz beam onto the receiver antenna. One complete time-domain waveform is collected for each random pattern.*

pixels in the image, i.e., $M < N^2$, and can still reconstruct the object perfectly, through an optimization procedure as described in references [8,9]. The THz Fourier imaging scheme using CS and phase retrieval in Chapter 3 uses a random subset of the Fourier basis as rows of Φ . Here, the single-pixel imaging method chooses a set of vectors, whose entries are randomly picked to be 1 or 0 with equal probability, as rows of Φ [60]. In other words, for each row in Φ , only a random subset (approximately half) of the pixels are set to unity (100% transmission), while the remainder are set to zero (no transmission). Thus, the terahertz beam traveling from the object to the detector is filtered by randomly blocking a subset of the spatial wave front.

4.2 Imaging experiment

Figure 4.1 illustrates the imaging setup, which consists of a THz transmitter/receiver pair (fiber-coupled photoconductive antenna), a planar screen with a random pattern

of blocked pixels, and two lenses. The THz beam, after passing through the object mask and the random pattern, is collected at the receiver. The positions of the screen, the focusing lens and the receiver along the beam path are calculated according to the lens law, in order to efficiently focus the THz beam onto the receiver antenna. The object mask is made of (opaque) copper tape on a transparent plastic plate. In this paper, our object mask has a hole shaped as a Chinese character which means “light”, 1.5 cm both by height and width, as shown in Figure 4.2(a). The screens used for this experiment are a set of four hundred random patterns printed in copper on standard printed-circuit boards (PCBs). Printed on a uniform grid on the PCBs, each pattern contains 32×32 pixels. The size of each pixel is $1\text{mm} \times 1\text{mm}$. A “copper” pixel corresponds to pixel value zero on the random pattern, while a pixel without copper corresponds to the value one, since the PCB material is fairly transparent to the THz beam. Each PCB moves on an automatic translation stage to change from one random pattern to another to ensure accurate alignment. For each random pattern, the system acquires one THz waveform, consisting of the superposition of the radiation transmitted through all of the un-metallized pixels.

In CS, every row of the measurement matrix Φ (that is, every random pattern) is used to form only one measurement, consisting of a complete time-domain waveform. In amplitude-only imaging, for each random pattern, the magnitude of the detected THz waveform at a particular frequency is extracted to obtain one CS measurement. For complex or phase imaging, the real and imaginary components of the THz waveform at the selected frequency form one CS measurement.

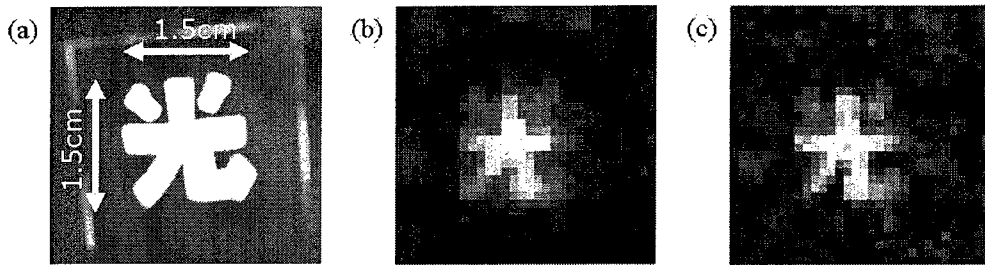


Figure 4.2 : (a) White-light image of object mask shaped as the Chinese character "light". Terahertz images reconstructed via compressed sensing using (b) 300 and (c) 600 magnitude measurements, which are respectively about 30% and 60% of the total number of image pixels. Both figures display a 32×32 image and the pixel size is $1\text{mm} \times 1\text{mm}$.

4.3 Imaging results: Amplitude-only images

The amplitude-only imaging experiment measures the magnitude of the detected THz waveform at a frequency of 100 GHz ($\lambda = 3$ mm), because near this frequency the incident THz beam is large enough to illuminate the entire object and has a high spectral amplitude. Figure 4.2(b) and (c) show the CS reconstruction results, 32×32 images of the object in Figure 4.2(a) with $1\text{mm} \times 1\text{mm}$ pixel size, using 300 and 600 measurements respectively. The reconstruction algorithm uses minimization of the total variation (min-TV) [9]. Appendix A describes the details of a fast algorithm for min-TV, called the Fast Total Variation deconvolution (FTVd), which uses less than 10 seconds to compute the reconstruction results in Figure 4.2 in Matlab on a standard PC [58]. Our system accurately reconstructs both the size of the object and its millimeter-scale features. Reconstruction using more measurements yields a sharper image but also adds some artifacts. Sources of noise include laser power fluctuation and alignment errors between patterns.

Figure 4.3 plots the normalized mean-squared error (MSE) of the reconstructed images of the object in Figure 4.2 using different number of masks (CS measurements).

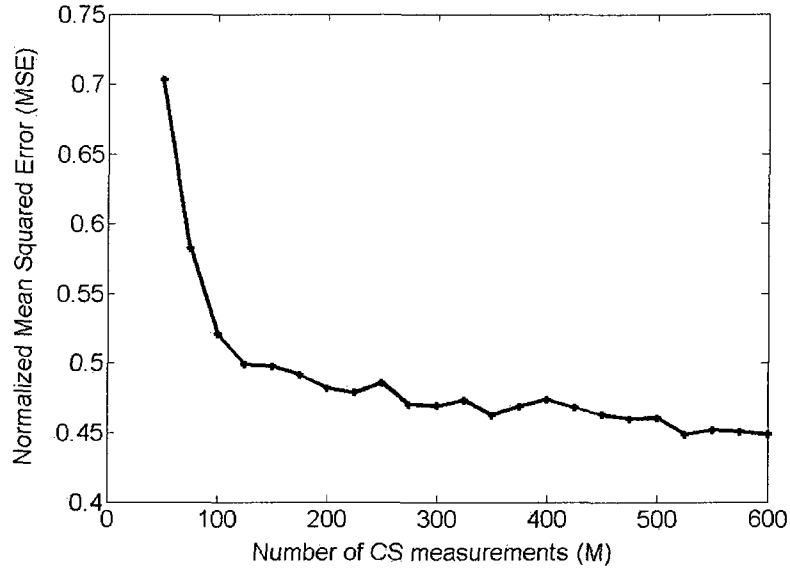


Figure 4.3 : As the number of measurements (M) used in CS increases, the mean-squared error (MSE) between the magnitudes of the reconstructed image and the reference image for the object in Figure 4.2, normalized by the squared energy of the reference image, decreases. The MSE decay is fast from 50 to 100 CS measurements. After the number of CS measurements exceeds the “sparsity” of the object, the decay flattens out.

Due to the reduced rate of convergence of the min-TV reconstruction algorithm for number of CS measurements below 250, the reconstruction uses the minimization of the l_1 -norm in the wavelet basis [8] for the results in Figure 4.3. The normalized MSE of each reconstructed image is computed as follows,

$$MSE = \frac{\sum_i (X_r(i) - X(i))^2}{\sum_i X(i)^2}, \quad (4.1)$$

where the summations are across all image pixels, X_r is the reconstructed image and X is a 32×32 greyscale reference image downsampled from a digital photograph of the object. The MSE sharply decreases from 50 to 100 CS measurements and then decays more slowly afterwards. The shape of this decay curve is dependent on the

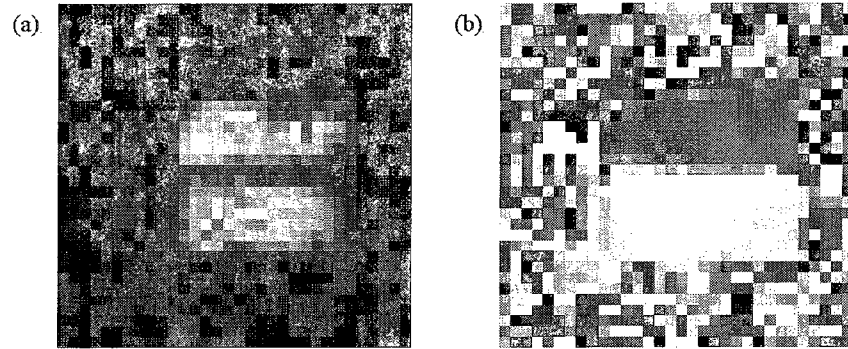


Figure 4.4 : *Compressed sensing reconstructions of (a) the image amplitude and (b) the phase, using 400 (complex) measurements. Here, the object is a rectangular hole in an opaque screen, covered with a (transparent) plastic plate. The plate covering the upper half of the hole is thicker than the lower half. The reconstructed phase image exhibits this contrast much better than the amplitude image.*

sparsity of the object in the reconstruction basis and on the system noise [59]. In general, this decay is fast until the number of measurements reaches the sparsity level of the object. The experimental result is consistent with this trend.

4.4 Imaging results: Complex images

There have been very few implementations of CS systems capable of acquiring and reconstructing complex image data. Since pulsed THz systems are well-known for providing spectroscopic phase information, this experiment demonstrates the capability in our single-pixel system, using CS algorithms specifically designed to reconstruct complex images [57]. The object to be imaged consists of a simple rectangular hole, half of which is covered by a transparent plastic plate. For each random pattern, both the magnitude and phase of the THz radiation at a single frequency (again, 100 GHz) are determined. CS reconstruction with 400 measurements using the SPGL1 algorithm (see [57]) yields the image amplitude and phase shown in Figure 4.4. While

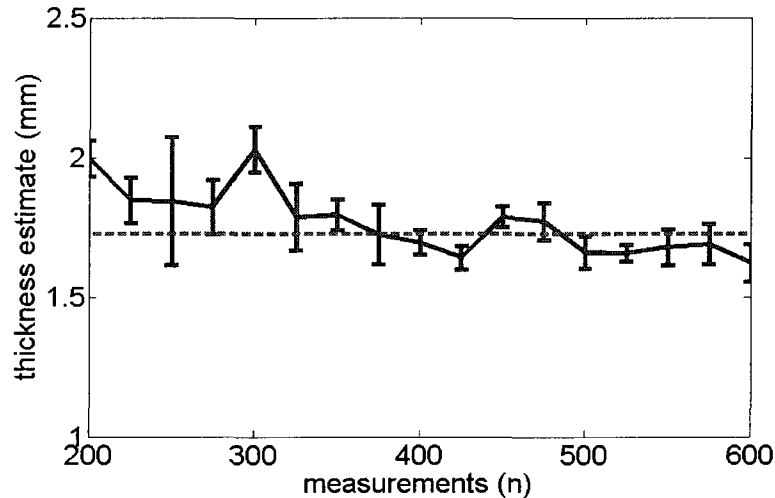


Figure 4.5 : *The estimated thickness of the plastic plate, versus number of measurements (n) used in CS reconstruction for the object in Figure 4.4. Dashed line indicates the actual thickness difference (1.73 mm), as determined using a micrometer. The thickness estimates rapidly converge to the correct answer with increasing n .*

the amplitude image shows almost no contrast, the phase image shows a sharp contrast between the upper and lower halves of the rectangular aperture. The thickness difference (Δd) can be estimated from the measured phase difference ($\Delta\theta$) according to $\Delta\theta = \frac{\omega(n-1)\Delta d}{c}$, which is valid since the plastic is essentially dispersionless. The acquired data follows a linear relationship of $\Delta\theta$ versus frequency, and the slope of that line is used to estimate Δd . Figure 4.5 shows the estimated value, for an increasing number of CS measurements from 200 to 600. Compared to the value $\Delta d = 1.73$ mm determined with a micrometer, Figure 4.5 shows that the estimation results rapidly converge to the correct answer, even for a small number of CS measurements. Another reconstruction algorithm which assumes smoothness in the phase image yields even better results [72]. Other recently developed algorithms for complex images might even achieve better reconstruction results [73].

4.5 Discussion

The single-pixel, pulsed THz camera described in this chapter does not rely on raster scanning, or a source/detector array, but uses random patterns for imaging. Based on the theory of CS, the system is capable of recovering a 32×32 image of a rather complicated object with only 300 measurements ($\sim 30\%$). This significant reduction in number of measurements used for CS image reconstruction can speed up the acquisition tremendously compared to traditional raster-scan systems. Moreover, the reconstruction in Section 4.3 from only the amplitude measurements at a single frequency is equivalent to imaging using a continuous-wave (cw) THz source. If we apply this method directly to cw THz systems, we could use a more sensitive single-pixel detector, such as a Schottky diode, and thus reduces the source power requirement dramatically compared to imaging with existing multi-pixel detector arrays.

Unlike its optical counter-part which measures only intensity [60], the pulsed THz camera can reconstruct complex images. In this case described in Section 4.4, acquisition of the entire THz waveform is necessary. The system thus obtains hyperspectral and phase information at the expense of lower imaging speed due to the mechanical movements of the delay line.

Currently, the major limitation of our setup is the slow translation of one random pattern to another. However, it is clear that other schemes for binary spatial modulation of a THz beam, driven either optically or electrically, can operate extremely rapidly and with no mechanical moving parts. Chapter 5 describes the proposed modulation scheme in this thesis, which should allow the acquisition of sufficient information for image reconstruction at a rate compatible with video imaging.

Chapter 5

Terahertz spatial light modulator (SLM)

In the past decade, much research effort has been focused in the area of THz generation and detection [74, 75], while many functional devices for direct manipulation and processing of THz radiation are still lacking. One example is a spatial light modulator (SLM) for THz beams. SLMs allow the optical or electrical control of the spatial transmission (or reflection) of an input light beam, and thus the ability to redirect or encode information in a wave front. Such devices are key components for many optical and optoelectronic systems, with applications in optical processing, optical interconnections, image display and real-time beam steering [76, 77]. Real-world examples of SLM include liquid crystal display (LCD) projector, and the Texas Instruments (TI) digital micromirror device (DMD) [78]. This technology, if extended to the THz region of the spectrum, can benefit exciting applications in THz imaging and communications [79, 80]. For instance, the major speed limitation for the single-pixel THz imaging system in Chapter 4 is the slow translation of random patterns on PCBs from one to another. A high-speed SLM would be ideal for encoding random spatial patterns into the wave front of a THz beam for this imaging application.

The construction of a THz SLM requires an array of small THz devices that can independently control the transmission of a THz beam at their respective array positions. Traditional technologies for SLMs in the optical regime [76, 81], which use liquid crystals, magneto-optic effects or deformable mirrors, do not operate efficiently in the THz regime because of the lack of materials with the desired THz response and/or the

size mismatch between micro-machined devices and THz wavelengths. THz modulators based on quantum-well structures either require cryogenic cooling [82] or have a poor modulation depth [83]. Other previous efforts in building THz modulators also yield modulation of only a few percent [84] or require high operation voltage [85].

This chapter reports the construction of two THz SLMs based on the use of active THz metamaterials [11,12,86,87]. This metamaterial device consists of a planar array of sub-wavelength-sized split-ring resonator (SRR) elements fabricated on epitaxial n-doped GaAs grown on a semi-insulating GaAs substrate [11] (see Figure 5.1(a) and (b)). The control of the metamaterial resonance is realized by the depletion of substrate charge carriers upon voltage bias which in turn changes the loss at the capacitive split gaps and therefore the oscillator strength of all of the individual SRR elements within a pixel. The device enables an amplitude modulation depth of ~ 3 dB under a relatively small bias voltage (16 volts) at room temperature [12]. Moreover, fast modulation, in the megahertz range, is achievable [86]. The design of such metamaterial devices is flexible because the resonant frequency can be tuned by changing the geometry and dimensions of the SRR elements [88]. Compared to existing THz modulators [82–85], the metamaterial-based devices are very promising for the construction of a high-speed THz SLM.

5.1 Metamaterials

Metamaterials are artificially constructed materials which exhibit electromagnetic properties not readily found in nature [89]. A metamaterial is usually a collection of structures whose size and spacing are much smaller than the wavelength of the electromagnetic radiation it interacts with. The electromagnetic response of this artificial material, or metamaterial, can be collectively characterized two macroscopic electro-

magnetic parameters: the electric permittivity, ϵ , and the magnetic permeability, μ , as if it is a homogeneous material. In 1999, early research invented metamaterials based on conducting elements designed to provide a magnetic response at microwave and lower frequencies [90]. These non-magnetic structures consists of arrays of wire loops, which have a self-capacitance and self-inductance that create a resonance under an external magnetic field.

In the literature, metamaterials have demonstrated special electromagnetic behaviors such as artificial magnetism and negative refractive index. According to the Snell's Law, beams will be deflected on the same side of the normal upon entering a metamaterial with negative refractive index. Such metamaterials designed at microwave frequencies, composed of negative permittivity and negative permeability, have led to intense theoretical, computational and experimental studies of exotic phenomena, such as perfect lensing and cloaking [91–93]. Artificial magnetism at microwave and THz frequencies has been demonstrated with SRRs [90]. This metamaterial, designed with a magnetic resonance in the mid-THz region, between 1 and 3 THz, provides a strong magnetic response not readily available in conventional materials [94]. This chapter will focus on the use of SRRs in the construction of a THz SLM.

5.2 First-generation 4×4 SLM design

The first demonstration of a THz SLM has 4×4 pixels, where each pixel is a 4×4 mm² array of metamaterial SRRs, as shown in Figure 5.1(c). The SRR elements have 200 nm gold thickness, 4 μ m line width, 2 μ m split gap spacing, 66 μ m outer dimension and 76 μ m period such that the device has a resonant transmission at 0.36 THz upon application of a voltage. Each pixel (consisting of approximately 2500 SRRs) is independently controlled by an external voltage across a 1×1 mm²

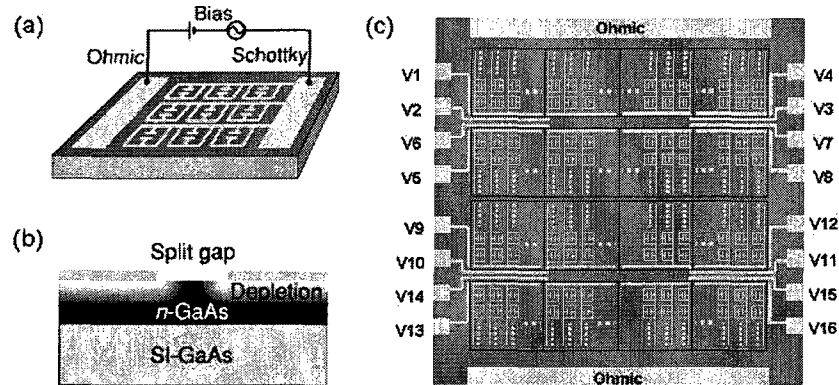


Figure 5.1 : (a) Each single pixel on the THz SLM contains a $4 \times 4 \text{ mm}^2$, ~ 2500 element array of metamaterial SRRs. These elements are connected together with metal wires to serve as a metallic (Schottky) gate. An external voltage bias controls the substrate charge carrier density near the split gaps, tuning the strength of the resonance. (b) Diagram of the substrate and the depletion region near the split gap of a single SRR, where the gray scale indicates the free charge carrier density. (c) The THz SLM (not drawn to scale) is a 4×4 array of individual pixels in (a). Each pixel is independently controlled by an external voltage between the $1 \times 1 \text{ mm}^2$ Schottky electric pad and the ohmic contact.

Schottky electric pad and the ohmic contact. This device has low power dissipation, drawing only a few milliamperes of current even when all the pixels are dc-biased at 14 volts.

5.3 Experiments and results

Characterization of the THz SLM uses a THz time-domain spectroscopy system in a transmission geometry with fiber-coupled photoconductive antennae for both THz generation and detection. The linearly-polarized THz beam is collimated and directed towards the modulator with the polarization of the THz electric field aligned along the direction across the SRR split gaps. This setup is useful for evaluating the modulation depth of each SLM pixel, the crosstalk between pixels, and the collective switching

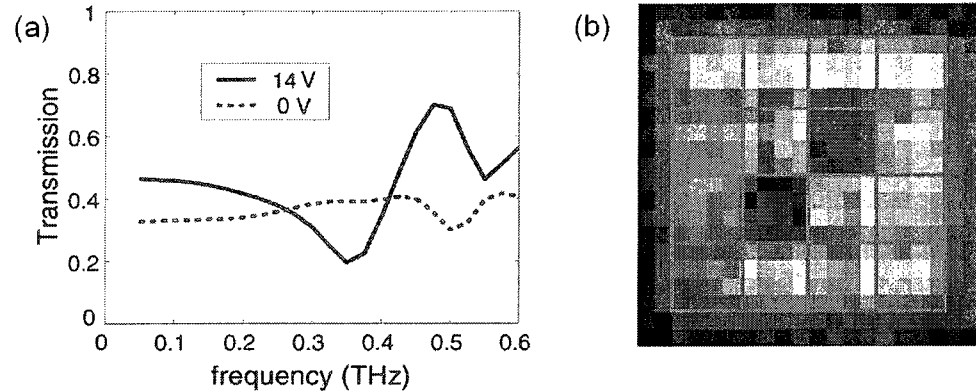


Figure 5.2: (a) THz amplitude transmission spectra for one of the 16 pixels of the THz SLM without voltage bias (dashed) and with 14V bias (solid). A large modulation depth is observed at 0.36 THz, the design resonant frequency. (b) A transmission image of the 4-by-4 array at 0.36 THz, with two pixels turned off (biased), and the rest turned on (zero bias).

of pixel groups at high speed.

5.3.1 Modulation depth

This experiment raster-scans the THz receiver across the beam, after it has passed through the modulator. The substrate lens of the receiver antenna is covered by a metal mask with a 1-mm aperture to improve the spatial resolution of the measurement. At each receiver position, THz waveform acquisition uses an optical chopper in the THz beam and a lock-in amplifier to filter the signal from the photoconductive antenna. Figure 5.2(a) shows the typical transmission spectra for one of the 16 pixels in the “on” and “off” configurations, i.e., under a dc bias voltage of 0 or 14 volts, respectively. Observed for all 16 pixels is an amplitude modulation depth between 35% and 50% at the design resonant frequency of 0.36 THz. Shown in Figure 5.2(b) is the transmission image of the 4-by-4 modulator array at 0.36 THz, with two pixels

turned off (biased) and the rest turned on (zero bias).

5.3.2 Crosstalk

To investigate the amount of crosstalk among the pixels in our THz SLM, this experiment does not use an optical chopper and instead modulate only certain pixel elements directly by applying a 3-kHz square-wave ac voltage bias, alternating between 0 and 14 V. Using a lock-in amplifier referenced to this square wave, combining the detected THz signal at every receiver position of the raster-scan produces a transmission image (Figure 5.3 inset). Signals with the largest amplitudes are concentrated at the two modulated pixels, with only a small amount of crosstalk in the surrounding pixels. To measure system noise requires another raster-scan with all pixels unbiased and unmodulated (while the lock-in amplifier is still referenced to the square wave voltage frequency). From the first data set, $\frac{N+C}{S}$, the ratio of the signal power at the surrounding un-modulated pixels (due to both crosstalk, C , and noise, N) to the signal power at the modulated pixel, S , is calculated for each frequency (dotted curve in Figure 5.3). Then, $\frac{N}{S}$, the ratio of the noise power from the second data set to S from the first data set is calculated (dashed curve). The difference between the two ratios gives the crosstalk level, independent of the system noise. This procedure is necessary because the crosstalk is so small as to be nearly indistinguishable from the noise.

As shown in Figure 5.3, the crosstalk level (solid curve) is larger (-15 dB) at lower frequencies due to diffraction effects, but drops to around -30 dB near 0.33 THz. Above this frequency, quantifying the amount of crosstalk becomes challenging because the noise-to-signal ratio increases due to the decreasing THz spectral amplitude, making the crosstalk indistinguishable from system noise. As a result, this

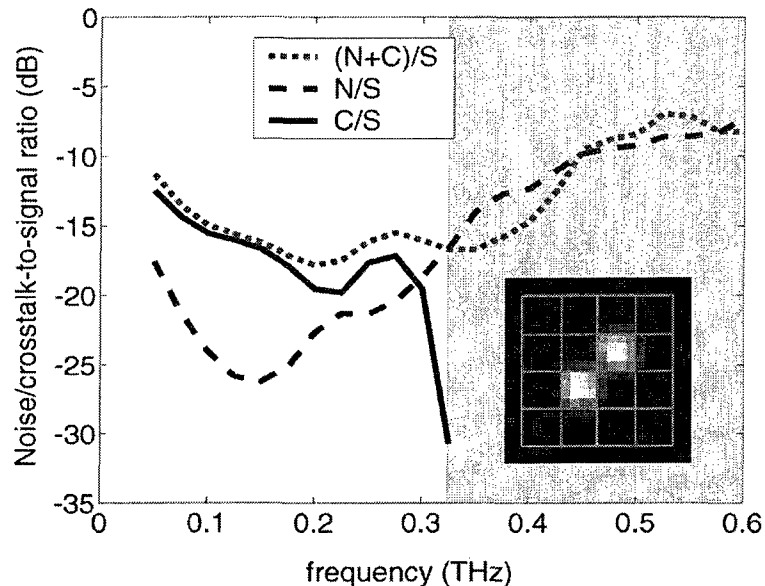


Figure 5.3 : Noise-to-signal power ratio (dashed) and noise-plus-crosstalk-to-signal power ratio (dotted) across frequency, from which we obtain the crosstalk level (solid). Above 0.33 THz (in the shaded area), crosstalk is buried in noise, and is therefore unmeasurable. These ratios are calculated from their corresponding transmission images of the 4-by-4 array of the THz SLM at every frequency. In the inset image at 0.36 THz, two pixels are under a square voltage bias and the rest are unbiased. A THz modulation (differential) signal is measured at each pixel using the lock-in amplifier referenced to the square voltage.

measurement is an upper limit on the crosstalk at the device operating frequency.

5.3.3 Switching performance

To provide an illustration of the dynamic switching capability of the THz SLM, this experiment modulates certain pixel elements for two distinct configurations. Shown in the insets of Fig 5.4 are two double-slit configurations. The white pixel elements are driven by a 3-kHz square wave varying between 0 and 14 volts, which is also used as the reference for the lock-in amplifier. The array elements shown in gray

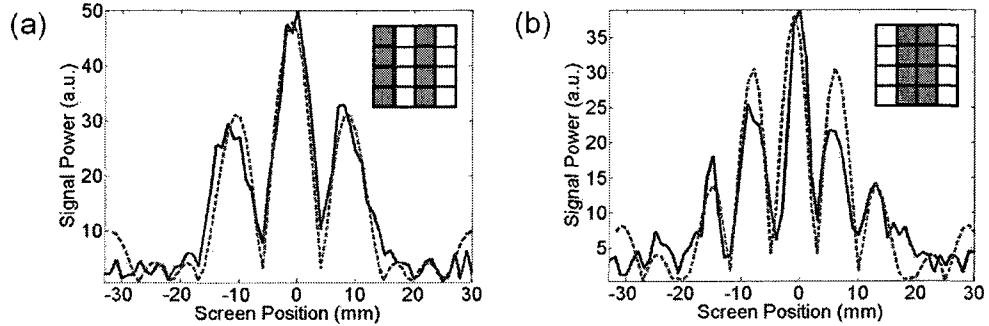


Figure 5.4 : Measured (solid curves) differential fringe patterns produced by the transmission of the THz beam through the THz SLM in two double-slit configurations, compared with analytical calculations (dashed curves). The insets show the “on” and “off” configurations of the 16 pixels, with zero bias on the gray pixels, and the white pixels modulated with a 3-kHz square signal alternating between 0 and 14V.

are unbiased. After focusing the transmitted THz wave front with a lens, the THz detector (with a 1 mm aperture) scans along a line in the focal plane of the lens, across a 64 mm interval. Figure 5.4 shows the measured differential fringe patterns (solid curves) at 0.36 THz for the two double-slit configurations. These have the same slit sizes ($b = 4$ mm) but different slit separations ($a = 8$ mm and 12 mm respectively in Figure 5.4 (a) and (b)). As expected, the fringes appear at distances, multiples of $\frac{\lambda f}{a}$, away from the central fringe. Here, λ is the observation wavelength, f is the focal length of the focusing lens and a is the slit separation. Analytical calculations of the double-slit diffraction pattern, assuming a plane wave illumination, best fit the measured data with $a = 9.8$ mm and 13.8 mm respectively for the two configurations, and $b = 5$ mm (see dashed curves in Figure 5.4). When using metal slits of the same dimensions as those of the slits formed by the modulator in a direct observation of the diffraction fringes, similar values for these fit parameters are observed. This indicates that the differences between the fit parameters and the actual geometrical dimensions

of the double slit are a result of the fact that the illuminating THz beam is not an ideal plane wave. To our knowledge, this is the first demonstration of fast dynamical modulation of a THz wave front.

5.4 Second-generation 32×32 SLM design

The first-generation SLM only has 16 pixels. Imaging and other SLM applications such as terahertz beam focusing and beam steering require a terahertz SLM with a larger number of pixels.

The second-generation terahertz SLM contains a 32×32 array of pixels, where each pixel is a 1.062×1.062 mm² array of metamaterial split-ring resonator (SRR) elements, as shown in Figure 5.5. More precisely, each pixel has an active area of $880 \mu\text{m} \times 860 \mu\text{m}$, which comprises of 100 metamaterial SRRs (see Figure 5.5(b) and 5.6(a)), and is separated from each neighboring pixel by a $200\text{-}\mu\text{m}$ space filled with connecting wires. The connecting wires between the pixels are $6 \mu\text{m}$ in width and $4 \mu\text{m}$ apart. The breakdown voltage of air is above 300 V for gaps larger than about $5 \mu\text{m}$, and it decreases linearly with gap length. Thus, the SLM with $4\text{-}\mu\text{m}$ gaps between the wires should be safe at the intended operation voltage, 16V. The SLM design is 4-fold symmetric. The 256 schottky electric pads on each side of the SLM control all the pixels in the respective triangular quadrant. The ohmic contacts placed at the four corners of the SLM are connected together by wires interdigitated between the pixels. The fabricated chip is $4\text{cm} \times 4\text{cm}$ in size, and $635\text{-}\mu\text{m}$ thick.

The design of the second-generation terahertz SLM uses SRRs with split gaps located at the four outer corners, as shown in Figure 5.6(b). Each SRR element is $88 \mu\text{m} \times 86 \mu\text{m}$, and has $200 \mu\text{m}$ gold thickness, $6 \mu\text{m}$ line width, $2 \mu\text{m}$ split gap spacing such that the device has a resonant transmission around 0.4 THz upon application of a

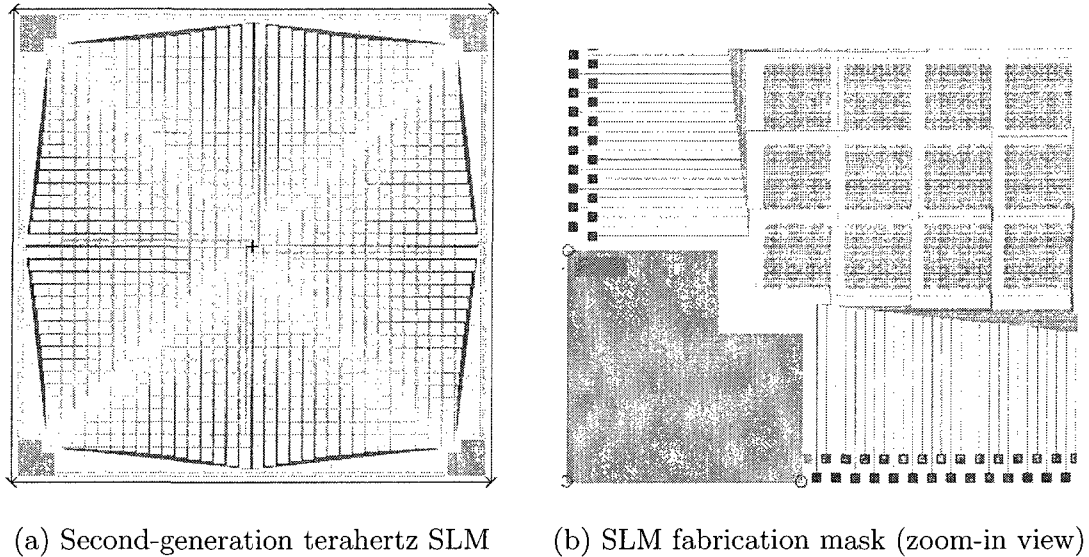


Figure 5.5 : (a) The second-generation terahertz SLM is a 32×32 array of individual pixels in Figure 5.6(a). Each pixel is independently controlled by an external voltage between the respective Schottky electric pad and the ohmic contacts (L-shaped pads at the four corners). The 256 Schottky pads on each side control all the pixels in one quadrant (triangular-shaped). (b) The active area of each pixel is $880 \mu\text{m} \times 860 \mu\text{m}$ and the spacing between pixels is about $200 \mu\text{m}$. The connecting wires between the pixels are $6 \mu\text{m}$ in width and $4 \mu\text{m}$ apart.

voltage. Chen *et al.* demonstrate a 55% modulation depth in amplitude transmission at a 16V bias on a terahertz modulator based on this SRR design [12].

5.5 Characterization experiments and results

Characterization of the two identical second-generation THz SLM samples (SLM 1 and SLM 2) uses a terahertz time-domain spectroscopy system with fiber-coupled photoconductive antennae for both terahertz generation and detection. A control circuit system synchronizes the THz SLM with the terahertz measurement system (see Appendix B). Figure 5.7 (a) and (b) show the terahertz amplitude transmission

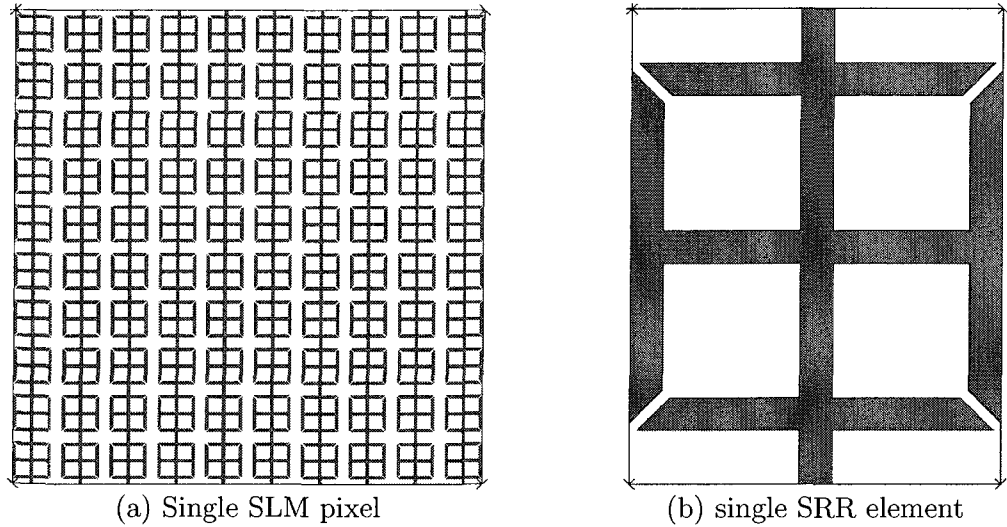
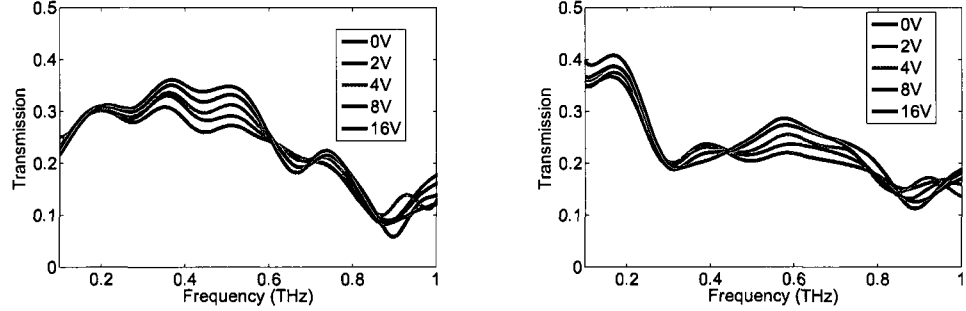


Figure 5.6 : Geometry of (a) one SLM pixel and (b) one metamaterial SRR element of the SLM. Each single pixel ($880\ \mu\text{m} \times 860\ \mu\text{m}$) contains a 10×10 element array of metamaterial SRRs. Each SRR element is $88\ \mu\text{m} \times 86\ \mu\text{m}$, with $6\ \mu\text{m}$ -wide metal and $2\ \mu\text{m}$ split gaps.

through a typical SLM pixel when the beam is linearly polarized parallel to and perpendicular to the connecting wires of the SRRs in the SLM respectively. Maximum modulation observed from 0V bias to 16V bias is 25% at 0.42 THz for terahertz polarization parallel to the connecting wires and is 20% at 0.37THz for the other polarization.

This experiment raster-scans the SLMs using a pinhole (with diameter less than 1mm) at the focal plane of the THz beam. At each pixel, the amplitude transmission waveforms are measured at both 0V and 16V biases. Figure 5.8(b) and 5.10(b) show the modulation depth (amplitude change from 0V to 16V) at 0.37 THz for each pixel of SLM 1 and SLM 2 respectively. In both cases, the terahertz polarization is perpendicular to the connecting wires in the SLM. The SLM pixels having modulation depth around 20% appear as dark image pixels, while the SLM pixels having zero



(a) Terahertz polarization perpendicular to connecting wires (b) Terahertz polarization parallel to connecting wires

Figure 5.7 : *Frequency-dependent terahertz transmission amplitude for a typical terahertz SLM pixel at various reverse gate biases for terahertz polarization (a) parallel to and (b) perpendicular to the connecting wires. Maximum modulation observed is 25% at 0.42 THz in (a) and is 20% at 0.37 THz in (b).*

modulation appear as bright image pixels. In both SLM 1 and SLM 2, some SLM pixels are broken (incapable of modulation).

5.6 Discussion

The first-generation THz SLM design, a 4-by-4 pixel array, successfully demonstrates a high modulation depth at the resonant frequency, uniformly across all and a negligible amount of crosstalk among pixels. Demonstrated by the interference patterns with a double slit configuration, the kHz-rate operation of this spatial modulator reveals great promise of its application to the single-pixel THz imaging system in Chapter 4. The THz SLM also operates at low voltages at room temperature and with low power consumption.

However, the characterization results of the second-generation THz SLM are not as satisfactory as the first-generation THz SLM. The circuit board of the second-

generation THz SLM control system has a few bad wire connections, which correspond to the scattered broken pixels occurring at the same image locations on both Figure 5.8(b) and 5.10(b). More importantly, some defects are observed under a microscope on both SLM 1 and SLM 2, which account for most of the broken pixels. Figure 5.8(a) and 5.10(a) show the location and sketches of some cracks, scratches, and fabrication problems on the SLM chips. The locations of defects match well with the locations of broken pixels. For example, in SLM 1, a scratch along the right side of the chip isolates most of the pixels in the triangular quadrant from their Schottky pads, therefore cutting off these pixels from the voltage supplies. More detailed microscope images reveal cracks in both SLM 1 and SLM 2 (see Figure 5.9(a) and 5.11) and fabrication defects in SLM 1 (see Figure 5.9(b)-(c)). During wire-bonding, the SLM chip is glued onto the circuit board, which is then screwed tightly onto the wire-bonding machine. The screwing force exerted on the sides of the SLM chip may have buckled it.

For proper wire-bonding, the wire-bonding company needs to place the SLM board at a fixed position on the wire-bonding machine at an exact height. During the first attempt to wire-bond a practice chip to the PCB, we provide them a PCB without cable connectors. When the company wire-bonds the two real SLM samples to the PCB with cable connectors, they find a difference in height because of the solder joints of the cables connectors at the bottom side of the PCB. While screwing the boards down more to compensate for the height difference, the boards might have slightly warped and exerted much pressure on the SLM chip, thus causing the cracks. To overcome this problem in the future, they suggest putting the cable connectors after wire-bonding, or cutting grooves into the workholder to accommodate the solder joints at the bottom of the PCB, or grinding down the solder joints. However, soldering

the cable connectors after wire-bonding may easily cause damage to the SLM chip. We prefer cutting groves into the workholder, and will discuss the procedural details with Nicholas Moses from VLSIP.

Future work involves investigation of the causes for the low modulation depth of the SLM pixels and the reasons for the fabrication defects. Measuring the doping density of the residual pieces of the wafer, on which our SLMs are fabricated, can ensure that the n-doped GaAs layer provide enough modulation. The next attempt to fabricate and package the THz SLM samples should avoid similar problems.

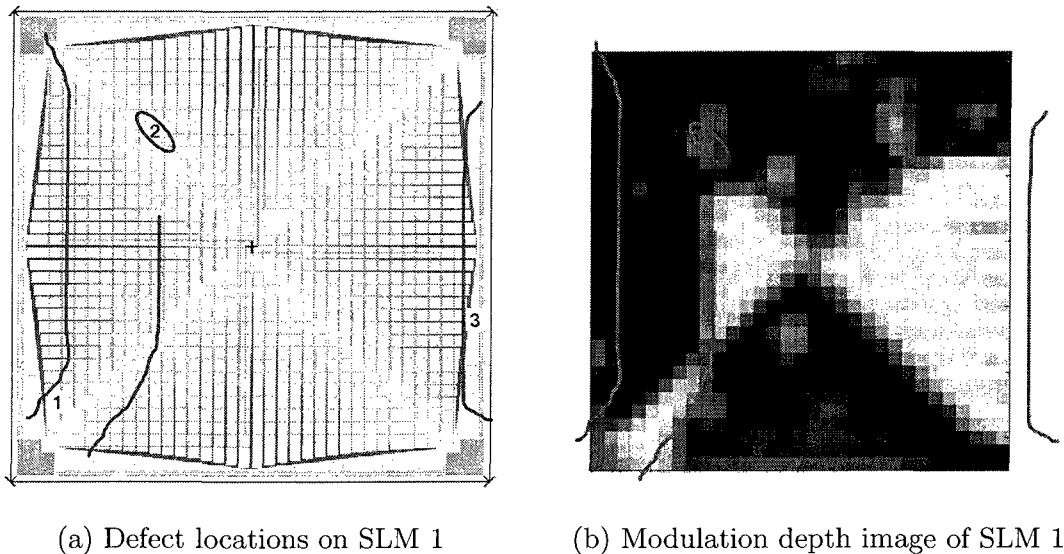


Figure 5.8 : (a) Locations of defects on SLM 1 observed under the microscope (see lines sketched on mask). (b) An 32×32 image of the modulation depth of the pixels on SLM 1, overlaid with sketches of defects in (a). At 0.37 THz, the SLM provides around 20% amplitude modulation at the darker regions on the image, and has zero modulation at the brighter regions. The defects cut off some SLM pixels from their Schottky pads, thus the SLM cannot provide any amplitude modulation at the corresponding pixel locations.

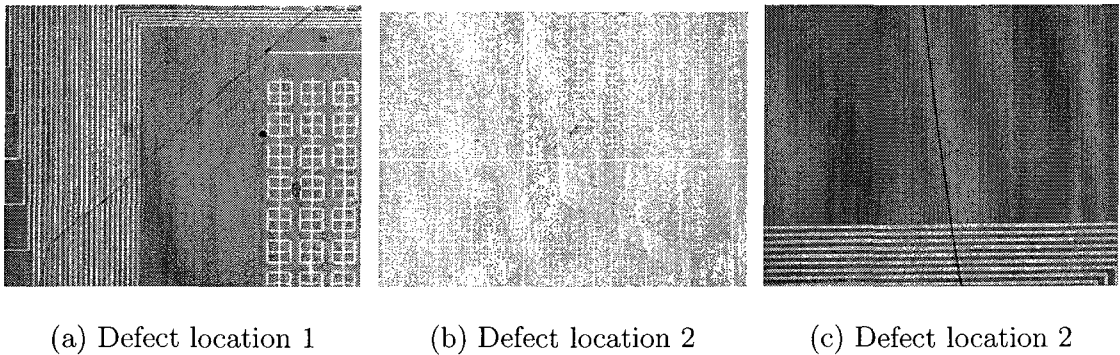


Figure 5.9 : Microscope images of defect locations on SLM 1 indicated on Figure 5.8(a). Location 1 has a crack whereas location 2 and 3 have fabrication defects.

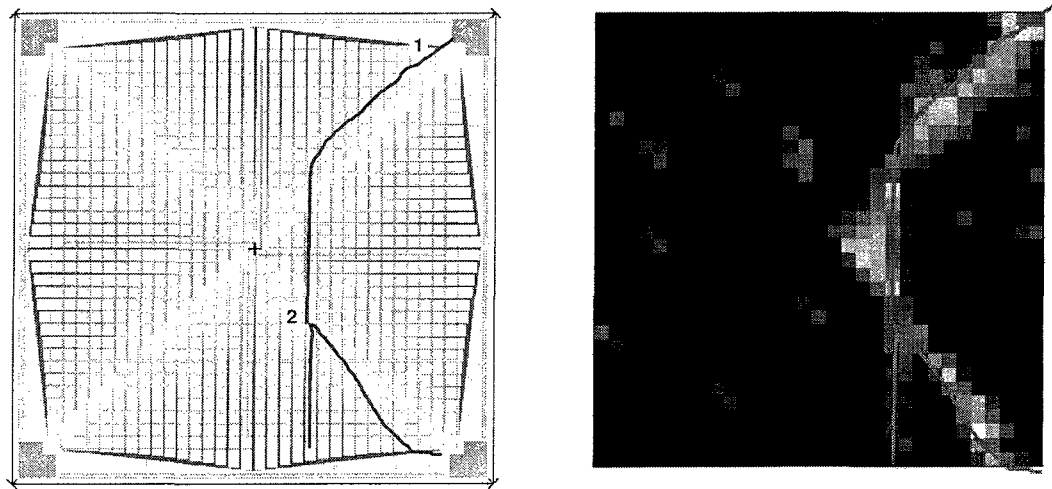
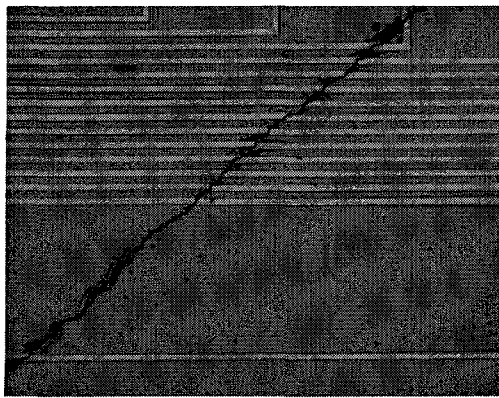
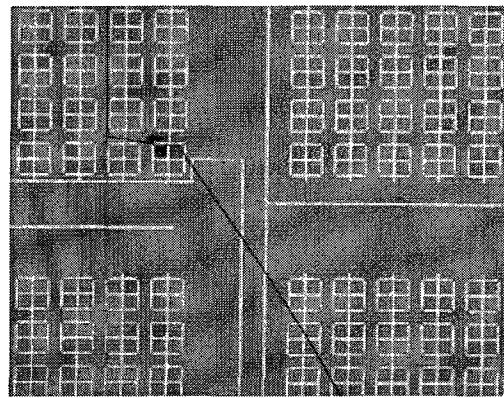


Figure 5.10 : (a) Locations of defects on SLM 2 observed under the microscope (see lines sketched on mask). (b) An 32×32 image of the modulation depth of the pixels on SLM 2, overlaid with sketches of defects in (a). At 0.37 THz, the SLM provides around 20% amplitude modulation at the darker regions on the image, and has zero modulation at the brighter regions. The defects cut off some SLM pixels from their Schottky pads, thus the SLM cannot provide any amplitude modulation at the corresponding pixel locations.



(a) Defect location 1



(b) Defect location 2

Figure 5.11 : *Microscope images of defect locations on SLM 2 indicated on Figure 5.10(a). A continuous crack runs through location 1 and 2 on SLM 2.*

Chapter 6

A future CS terahertz imaging system

6.1 Summary of results

In order to improve the image acquisition speed upon traditional raster-scanning systems, this thesis demonstrates two novel terahertz imaging systems based on compressive sensing: the CS Fourier THz imaging system and the single-pixel CS THz imaging system.

The CS Fourier THz imaging system successfully recovers the test object with pixel size 1.4 mm, using only a random subset of about 12% of the 4096 (64×64) uniform Fourier samples scanned at the focal plane of a lens. This image reconstruction result implies a 2/3 reduction of acquisition time compared to traditional raster scanning, with a slight loss in imaging resolution, if the system scans the receiver along a random path across a subset of pixels. The system also demonstrates successful image reconstruction with only the Fourier amplitude using compressive sensing phase retrieval. This setup could be useful for quality control applications, such as detection of point impurities in manufactured products, because Fourier-domain measurements are particularly sensitive to sharp point-like features.

While mechanical scanning of the receiver still limits the acquisition speed of the CS Fourier imaging system, the single-pixel CS THz imaging system does not rely on raster scanning, or a source/detector array; instead, it uses random patterns for imaging. Based on the theory of CS, the prototype system is capable of recovering a

32×32 image of a rather complicated object with only 300 measurements ($\sim 30\%$), but it still relies on mechanical moving parts. A fast spatial THz modulator for the binary modulation of the THz beam is required to realize a high-speed single-pixel CS THz imaging system.

Therefore, two spatial THz modulators are designed and implemented based on metamaterial split-ring resonators. The first-generation THz SLM design, a 4-by-4 pixel array, demonstrates a modulation depth of 35% to 50% at the resonant frequency, uniformly across all pixels, and a negligible amount of crosstalk among pixels. Demonstrated by the interference patterns with a double slit configuration, the kHz-rate operation of this spatial modulator can allow fast switching of random patterns for the single-pixel imaging system. The metamaterial spatial THz modulator operates under small voltage levels at room temperature and with low power consumption.

The second-generation design of the THz SLM has a much larger number of pixels (32×32) than the first-generation design. In order to independently control the 1024 SLM pixels, we build a control circuit system with a FPGA and voltage amplifying components. This system allows synchronization between the SLM control signals and the T-ray acquisition system. Initial THz experiments find only 20% modulation depth at each pixel of the second-generation THz SLM, and discover some fabrication and packaging defects on the THz SLM samples. Further investigation is needed to explain the low modulation depth, and to improve the fabrication and packaging procedures.

The major contributions of this thesis are the demonstration of the single-pixel THz imaging system, and the implementation and characterization of the THz SLM. When properly fabricated and packaged in the future, the second-generation THz

SLM will replace the mechanical switching of the random patterns in the prototype single-pixel imaging system and enable fast image acquisition. Combined with the latest CS image reconstruction techniques, we have made significant advances toward a high-speed THz imaging system, which will be much faster than the traditional raster-scan systems and more cost-effective than imaging systems based on detector arrays.

6.2 Future challenges

The immediate future steps following up the work described in this thesis are to fabricate new samples for the second-generation THz SLM, and to incorporate it into the single-pixel THz imaging system setup. The resulting system can demonstrate high-speed imaging through either switching on the SLM pixels one by one (equivalent to raster scanning pixel by pixel but without any mechanical movements), or switching the SLM pixels according to a set of random patterns (i.e., CS imaging). Yet, in the near future, to render a practical single-pixel CS imaging system, many challenges still lie ahead.

Besides imaging, other interesting experiments include using the SLM for THz beam focusing and beam steering, and for diffraction experiments with the SLM operating in various configurations such as multiple slits or a Fresnel zone plate. For these exciting applications, the first step is to improve upon the current THz SLM.

6.2.1 Terahertz SLM technology

The prototype second-generation THz SLM described in chapter 5 has a limited resolution, 32×32 with pixel size around $1\text{mm} \times 1\text{mm}$. For practical imaging applications, the number of pixels need to be at least 100 times more. Accordingly, the chip design

becomes more challenging because a single chip surface would not be able to provide enough space for *both* the pixels *and* their connecting wires to their respective schottky pads. Moreover, for such a large number of pixels, the current packaging of the SLM with many ribbon cables will be too bulky.

One solution is to design a THz SLM to be used for a reflection, instead of transmission, setup. The resulting chip will have multiple layers with the connecting wires beneath the pixels. Each pixel can be as small as the size of a single split-ring resonator, but cannot be smaller than the diffraction limit at the operating frequency. Not only will this design pack more pixels into a single chip, but also will allow more compact circuit and packaging similar to Texas Instrument’s digital micromirror device (DMD) [78].

Another drawback of the current metamaterial-based THz SLM is its limited modulation depth, and its narrowband operation. The modulation depth at each pixel is constrained by the depletion between the split gap of the resonator elements and the n-doped substrate. The highest modulation depth demonstrated is 55% at 0.81 THz [12]. The modulation occurs in a relatively narrow frequency range around the resonant frequency, making the device best applicable to continuous-wave THz systems. A more desirable SLM would be a DMD with mirrors optimized for a wide range of THz frequencies. This solution can provide broadband modulation at 100% depth, but loses the ability to tune the modulation depth at each pixel which is essential for applications such as THz beam steering and beam focusing.

6.2.2 Terahertz source power and receiver dynamic range

The performance of the single-pixel CS THz imager relies on its ability to detect a small change in the overall THz signal caused by the modulation at a single SLM

pixel. The smaller each SLM pixel is, the more the signal detection is prone to noise corruption. If either the THz source power or the detector sensitivity is too low, the signal-to-noise (SNR) performance of the system goes down. One trivial solution is to obtain more signal averages to increase the SNR, but the image acquisition time also increases proportionally. Using a lock-in amplifier can significantly eliminate system noise, but only works for amplitude measurements at a single time delay or is otherwise slow in the long scan mode. The best solution is to operate the CS imaging system with a high-power continuous-wave THz source, such as quantum cascade lasers, tuned at the resonant frequency of the THz SLM and with a highly sensitive single-point detector such as a Golay cell. Figure 6.1 qualitatively compares the source power and receiver requirements, and the speed performance of various imaging systems. The table assumes all imaging systems implementation with a continuous-wave THz source. If a pulsed THz source is used, the recently published electro-optic imaging technique using a time-of-flight demodulation detector array may be the least costly solution for fast imaging [39]. However, the power limitation in all pulsed THz sources is still a challenge to practical imaging. Alternatively, a tunable continuous-wave source may provide enough power for the single-pixel CS imaging system if hyperspectral information is desired. More research effort is still required to build a practical CS imaging system with continuous-wave THz systems and to compare its performance with the pulsed THz system used in this thesis.

More importantly, in order for this CS imaging scheme to have comparable performance to imaging using a microbolometer array, the single-pixel THz detector needs to have a dynamic range $\frac{N}{2}$ times the dynamic range of a single element in the detector array, where N is the number of image pixels [10]. If a single-pixel THz detector can achieve this desirable dynamic range with better signal sensitivity, the CS

	Raster Scan	CS Fourier	Single-pixel (CS)	Detector array
acquisition speed (potential)	LOW	MEDIUM	HIGH	REAL-TIME
Receiver requirement	Single-pixel detector	Single-pixel detector	Single-pixel detector	Micro-bolometer array
Source power requirement	LOW	MEDIUM	MEDIUM	HIGH
Hardware (comments)	Limit by slow mechanical movements	Limit by slow mechanical movements	Need high-speed SLM	low-sensitivity receivers; need high-power QCL

Figure 6.1 : Comparison of CS imaging systems with raster-scan and detector array systems. Assuming system implementation with a continuous-wave THz source, the single-pixel imaging system can provide high-speed imaging at room temperature with a reasonable hardware requirement.

imaging system will definitely be a suitable alternative to systems using focal plane detector array for high-speed imaging. A thorough investigation of the source and receiver characteristics of various THz systems is required to select the appropriate technology to implement the CS THz imaging system.

6.2.3 Terahertz spectroscopic and phase imaging

One of the major strengths of THz imaging, as compared to optical or infrared imaging, is the capability to obtain spectroscopic and phase information. Spectroscopic information is useful for identification of materials [52] whereas phase information provides depth information about the imaged object as in Section 4.4. However, a THz system with these capabilities usually needs to obtain an entire THz waveform,

thus increasing image acquisition time. Traditional pulse THz systems relies on the slow mechanical movements of the delay line to scan a time-domain waveform. Several faster alternatives exist such as asynchronous optical sampling [31,32] and single-shot chirp-pulsed detection [36–38]. If interested only in imaging phase information at one frequency, table-top continuous-wave systems based on diodes and frequency multipliers from Virginia Diode, Inc., which operates at 0.1THz to above 1THz, can be used to build CS imaging systems. Each of these systems have their advantages and drawbacks, which should be carefully considered before the implementation of a CS imaging system.

Last but not least, the ongoing research in the area of compressive sensing will continue to inspire new imaging techniques and applications [95]. For example, CS has only been used to reconstruct mostly 2-D THz images in this thesis. Further research in a third dimension, such as CS reconstruction of THz spectroscopic images or imaging/detection of cracks using lactose powder near its THz absorption frequency [96], will further enhance the imaging capability of future CS THz imaging systems. A great example of the application of CS to 3-D THz data is demonstrated in the context of pulse-echo mode THz reflectance tomography [97]. Development of reconstruction algorithms for complex THz data or THz phase images will also be important for CS applications in 3-D [72,73].

To conclude, this thesis is a first step to bridge the gap between the theory of compressive sensing and terahertz imaging. This piece of research, hopefully, will inspire future research in applying advanced signal processing theories to build practical imaging systems!

Appendix A

Implementation of minimization of total variation (min-TV) algorithm

This appendix describes the implementation of the Fast Total Variation deconvolution (FTVd) algorithm [58] used to generate the imaging results of the Chinese character “light” in Figure 4.2 for the single-pixel CS imaging system.

The CS reconstruction problem, in this case, based on the minimization of the total variation of the image x is given by,

$$\min_x TV(x) + \frac{\mu}{2} \|\Phi x - y\|^2, \quad (\text{A.1})$$

where $TV(x)$ is defined as $\sum_i \|D_{(i)}x\|$, with $\|D_{(i)}x\|$ being the total variation of x at pixel i , Φ is the measurement matrix, y is the acquired data, and μ is the regularization parameter to be chosen based on the problem. The FTVd algorithm approximates the minimization problem in (A.1) as

$$\min_{\mathbf{w}_i, x} \sum_i \|\mathbf{w}_i\| + \frac{\mu}{2} \sum_i \|\mathbf{w}_i - D_{(i)}x\|^2 + \frac{\mu}{2} \|\Phi x - y\|^2, \quad (\text{A.2})$$

where β and \mathbf{w}_i are new variables introduced into the optimization. Equation (A.2) can be solved by alternating minimization, where the w -subproblem contains the two leftmost terms in (A.2) and the x -subproblem contains the two rightmost terms in (A.2). The w -subproblem has a closed-form solution while the x -subproblem can be simplified into a least-square problem [58]. The original FTVd algorithm solves the

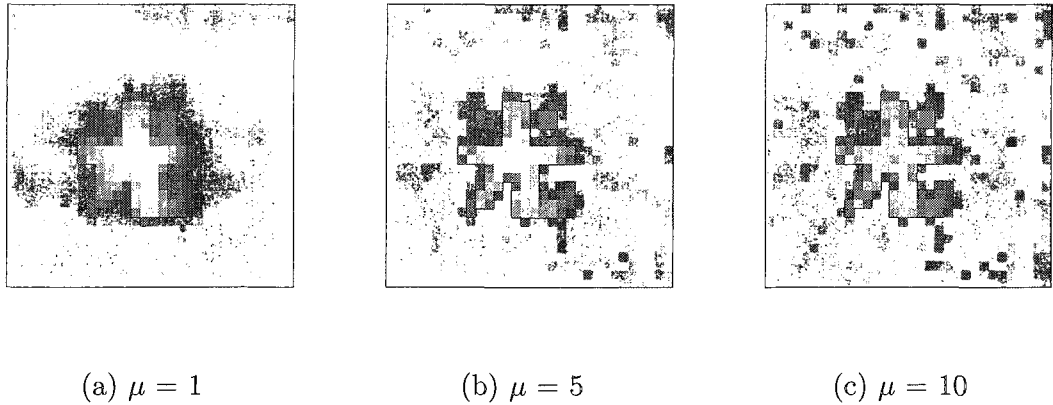


Figure A.1 : Test FTVd reconstruction results of the Chinese character “light” for the single-pixel CS imaging system for various μ and a maximum β of 1024. A smaller μ yields a smoother image while a larger μ gives a sharper but noisier image.

x -subproblem with the fast Fourier transform, applicable only when Φ is a Toeplitz matrix. Since the measurement matrix Φ used in the single-pixel imaging system is random, my implementation uses the matrix left division in Matlab to solve the x -subproblem. This implementation can be slow, but works for the small-size problem in this thesis. The TVL_3 algorithm should be a faster alternative for solving the reconstruction problem in (A.1) for general matrix Φ and even for complex data [73].

A quick note on choosing the optimization parameters, μ and β : The regularization parameter μ controls the weights between the smoothness (min-TV) assumption and the measured data used for the reconstruction. A smaller μ yields a smoother image while a larger μ usually gives a sharper but noisier image because the measured data is noisy (see Figure A.1). The FTVd algorithm uses a continuation for β (gradually increasing with the number of iterations), so it only requires an upper limit for β . For the test results used in this thesis, typical values for μ is between 1 and 10, whereas β should be powers of 2, between 256 and 1024.

Appendix B

Second-generation terahertz SLM control system

When designing the second-generation 32×32 terahertz SLM, not only the chip design itself, but also the wiring, packaging and control of the chip become challenging. The chip design needs to compact all the pixels, on-chip wires and bond pads to a chip of a reasonable size, while keeping metal parts at a safe distance from each other to avoid air breakdown at a voltage difference of 16V. Chip packaging should be able to accommodate over a thousand wire connections from the control circuit to a small chip, but, at the same time, allow movement on an optical table for making terahertz measurements. Automatic and synchronous switching of over a thousand SLM pixels at high speed and at the specified voltages require advanced digital circuit systems, and careful design of cable connections among the circuit boards. This appendix describes the details concerning this control circuit.

The second-generation SLM has 1,024 pixels. Individually switching on and off each pixel require a programmable control circuit. The current design of the control system consists of three circuit boards: a FPGA circuit which controls the switching of each SLM pixels and the synchronization between the SLM and the T-ray system, two line driver circuits which increase the voltage amplitude of each switching signal from 3V to 16V, and the SLM board which holds the SLM chip (see Figure B.1). The following sections describe each part of the control system in detail.

B.1 FPGA circuit

The FPGA circuit provides the digital logic to control every SLM pixel, and allows synchronization between these control signals and the T-ray acquisition system. This circuit is the AFX-FF1760 prototyping platform in Figure B.2, with the Virtex-5 LX330 FPGA mounted in the ZIF socket as in Figure B.3(a).

The Virtex-5 LX330 FPGA has the largest number of user-configurable input/output (I/O) pins, 1,200 I/O pins, among all the Xilinx FPGAs, thus this device can simultaneously control all the 1,024 SLM pixels. The FPGAs used for our experiments are generous donations from the Xilinx University Program (XUP). To mount the FPGA onto the ZIF socket, first put the FPGA in place with the vacuum handling tool, then press the socket inward to lock the FPGA into the ball-grid array (BGA) beneath.

The AFX platform downloads the program instructions from the computer to the FPGA through the USB-JTAG programming cable in Figure B.3(b). These instructions are written in Verilog programs. The AFX platform connects to the line driver circuit through IDSD cables manufactured by Samtec, Inc., receives a clock input from an external signal generator and outputs a synchronization signal to the T-ray acquisition system through BNC cables.

Detailed documentations of the Virtex-5 FPGAs and the AFX platform is available on the Xilinx webpage.

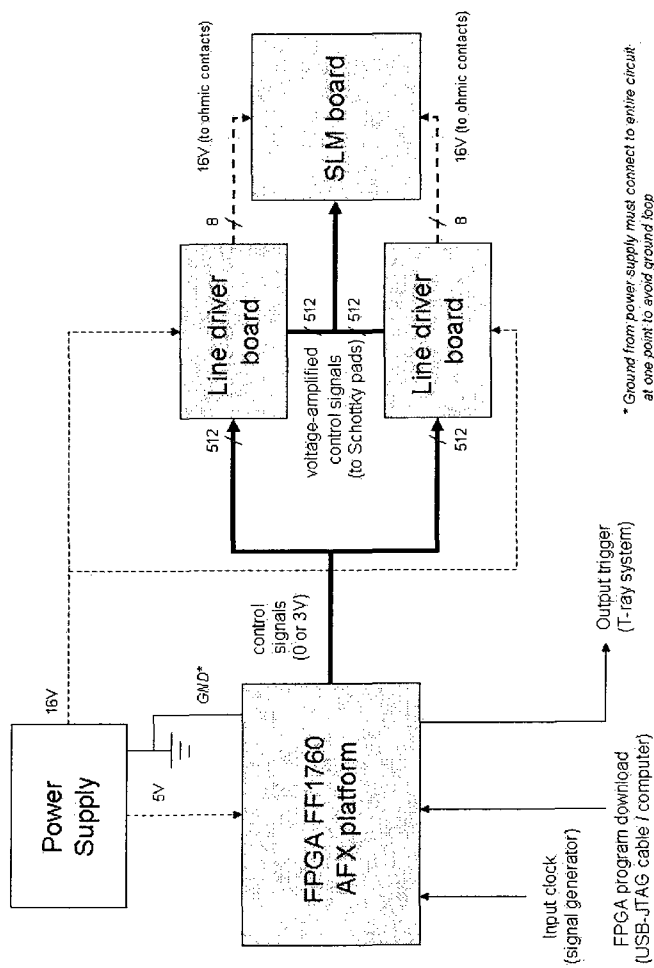


Figure B.1 : Terahertz SLM control system diagram. The control system consists of three circuit boards: the FPGA platform which controls the switching of each SLM pixels and the synchronization between the SLM and the T-ray system, two line driver boards which increase the voltage amplitude of each switching signal from 3V to 16V, and the SLM board which holds the SLM chip.

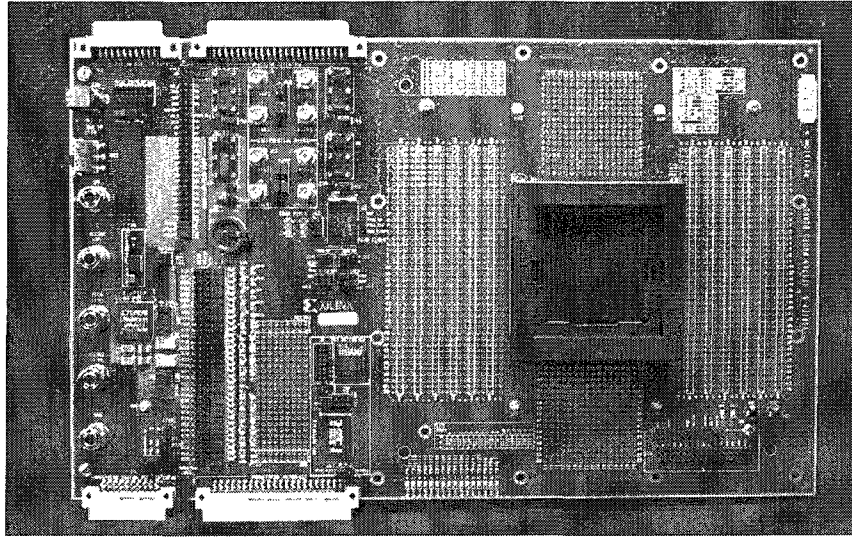


Figure B.2 : Xilinx AFX-FF1760 FPGA prototyping platform (before the Virtex-5 LX330 FPGA is mounted). The ZIF socket is convenient for the mounting and dismounting of the FPGA.

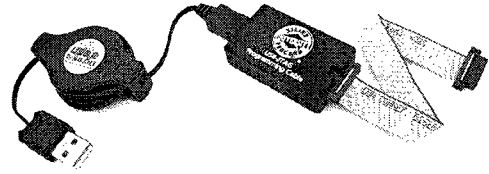
Caution: As shown in Figure B.1, the entire SLM control system must only connect to the ground of the power supply at one point. One way to do this is to first connect all the ground cables from the line driver boards to the ground of the FPGA circuit. Then, connect the ground of the power supply to the ground of the FPGA circuit, and avoid any other wire connections to the ground of the power supply.

Caution: The AFX platform and the FPGA are both electrostatic-sensitive devices. Please make sure to ground oneself before handling these circuits. Always check the current supplied to the FPGA on the power supply panel display to ensure proper FPGA operation. The standard current is between 1A and 1.5A for most programs used in the experiments.

Suggestion: The XUP USB-JTAG programming cable is fragile and should not be



(a) Xilinx Virtex-5 LX330 FPGA



(b) Digilent USB-JTAG programming cable

Figure B.3 : (a) The LX330 FPGA is one of the largest FPGA in the Virtex-5 family. It contains 1200 user-configurable I/O's, thus sufficient to control 1024 SLM pixels simultaneously. (b) The USB-JTAG programming cable connects the USB port of a computer to the JTAG port on the FPGA prototyping platform. The Xilinx ISE software programs the FPGA through this cable.

stretched too much. Another more robust but expensive version of the same cable (part number: HW-USB-II-G) is available on the Xilinx webpage.

B.2 FPGA Verilog programming

One can program the FPGA either in Verilog or VHDL language. The SLM control system has Verilog programs written for raster scanning, i.e., switching on each SLM pixel in a particular order, or for reading in and displaying SLM patterns from text files one by one, or other test programs for the SLM characterization experiments. The computer uses the Xilinx ISE software (Version 11.1) as the Verilog programming interface and for compilation of Verilog programs into bitstreams to be downloaded onto the FPGA. The two major user-written components of a ISE project are the

Verilog programming file (.v), which contains the code, and the UCF file (.ucf), which contains the assignments of the FPGA pins to the program variables. The UCF file for the SLM control circuit, i.e., the FPGA pin assignments to the SLM pixels, is fixed and is stored in the control computer. One should not need to reconstruct this UCF file in the future, but in case of future changes to the circuit, see Section B.3 for the procedure to match the FPGA pins to SLM pixels.

Compilation of a Verilog programs can take several hours sometimes, especially for programs using many FPGA pins. Once ISE generates the bitstream file (.bit) after compilation, the FPGA can download and use the bitstream next time without having to go through compilation procedure again.

More details of the ISE software is available on the Xilinx webpage. Contact the CMC Lab at Rice University for free download of the ISE software.

B.3 FPGA pin assignments

Arranged in a square array, the pinout description of the Virtex-5 LX330 FPGA is available on the Xilinx webpage. Notice that the FPGA pinout map has a 180° rotational symmetry, therefore, two identical line driver boards are designed for each side of the FPGA circuit.

The labelling for the SLM pixels is as follows: when the SLM board is oriented such that the white silkscreen box is on the right bottom corner (see Figure B.7), the pixel on the left top corner is pixel 1. Count downwards in ascending pixel number. Then, start counting again with the pixel at the top of the second column from the left as pixel 33. Stay with this counting pattern until reaching pixel 1024 at the bottom right corner of the SLM.

One may need to use an EXCEL sheet to keep track of the pin assignments from

one circuit board to another. Here describes the steps to map the pins and the pixels, i.e., to construct the UCF file:

1. From the schematics of the line driver board in Allegro Design Entry CIS, map the 512 FPGA pins to the corresponding SHF cable connector pins.
2. From the schematics of the SLM board, map each SHF cable connector pin to the corresponding PCB bond finger for the SLM chip.
3. Map each Schottky pads on the SLM chip to the corresponding SLM pixel according to the chip design in Figure 5.5 (mapping between the PCB bond fingers and the Schottky pads is straightforward).
4. Use this pin-to-pixel mapping to figure out the mapping for the 512 pins on the other side of the FPGA by its symmetry.

B.4 Line driver circuit

The line driver circuits amplifies each of the 1,024 control signal from the FPGA circuit from 3V to 16V, since each SLM pixel requires a 16V negative bias for maximum modulation. The line driver circuit provides +16V to the SLM ohmic contacts through the SLM board, and switches each of its output control signal between 0V and 16V.

As shown in Figure B.4, the line driver circuit board has a Zener diode and a fuse for basic circuit protection, a bypass capacitor for a cleaner DC signal, and cable connectors to connect from the FPGA circuit and to the SLM board. Each line driver board has 512 outputs, each to an individual SLM pixel. For each SLM pixel, the circuit performs independent voltage amplification through a bipolar-junction-transistor (BJT) and two transistors, as shown in Figure B.5. This circuit diagram

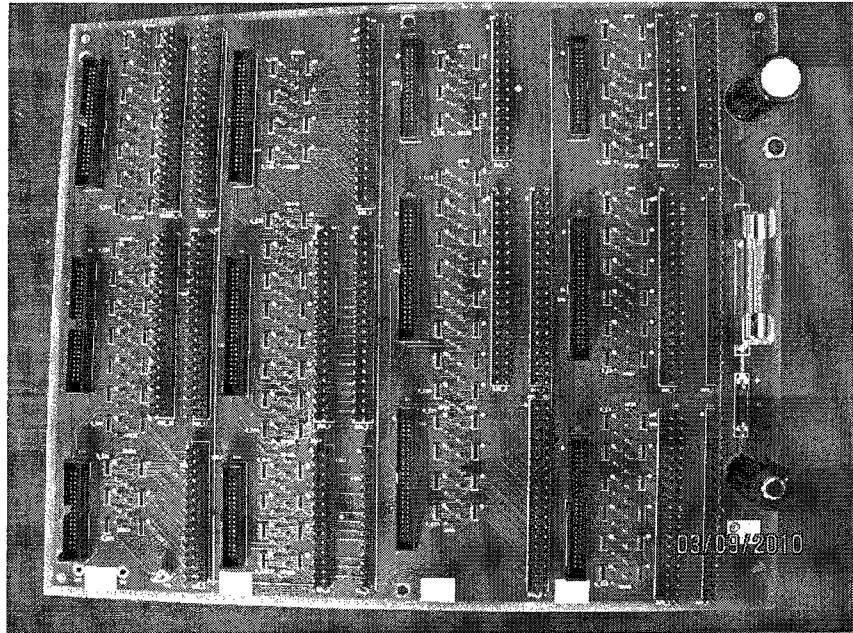


Figure B.4 : *Line driver circuit board, which amplifies the voltage amplitudes of 512 FPGA control signals from 3V to 16V. The circuit board contains two banana cable jacks, a Zener diode and a fuse for circuit protection, a bypass capacitor, connectors to connect from the FPGA circuit and to the SLM board, and 512 voltage-amplifying circuit made of bipolar transistors and resistors.*

models the SLM pixel as a diode and the cables as inductors. Resistor values are chosen to provide the correct voltage amplification and to draw reasonable current from both the FPGA pins and the 16V power supply. The larger R_C is, the less current drawn from the power supply but the switching becomes slower.

Here outlines the design procedure for the line driver circuit board.

1. Design the basic circuit model.
2. Determine all circuit components to use based on manufacturer, model, availability and packaging type.
3. Draw all component packages and the corresponding wire connections in the

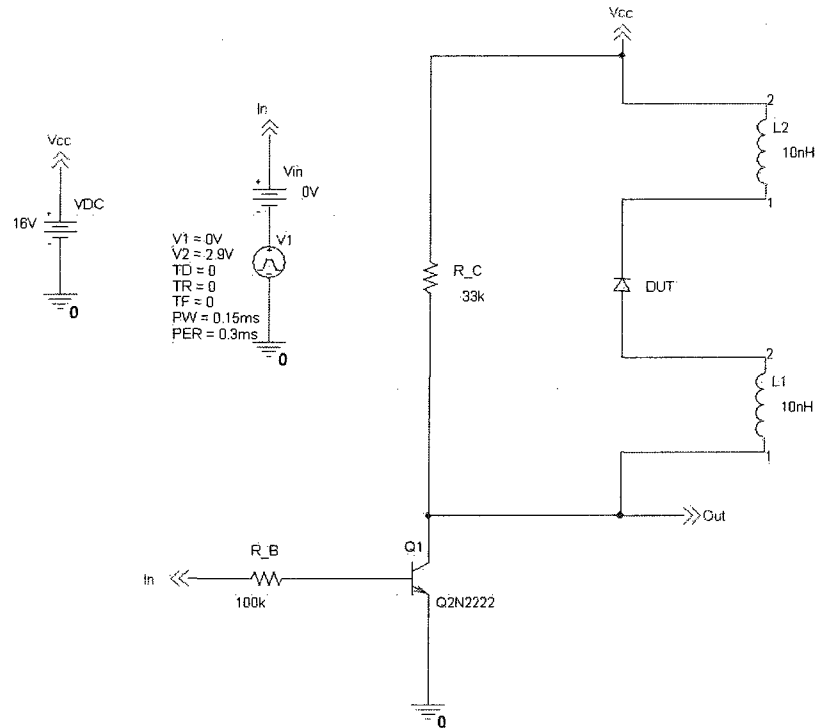


Figure B.5 : Bipolar-junction-transistor (BJT) set up as a common-emitter amplifier for voltage amplification. Each 3V control signal from the FPGA circuit acts as the input to one common-emitter amplifier, and the output passes onto each SLM pixel after being amplified to 16V.

schematic design program, Allegro Design Entry CIS.

4. Export the netlist of the schematics to be used in the PCB layout software, Allegro Cadence.
5. Layout the exact positions of the components and wires in Allegro Cadence.
6. Send layout files, generated in Allegro Cadence, to a company for PCB fabrication.
7. Purchase parts and send to a company for assembly.

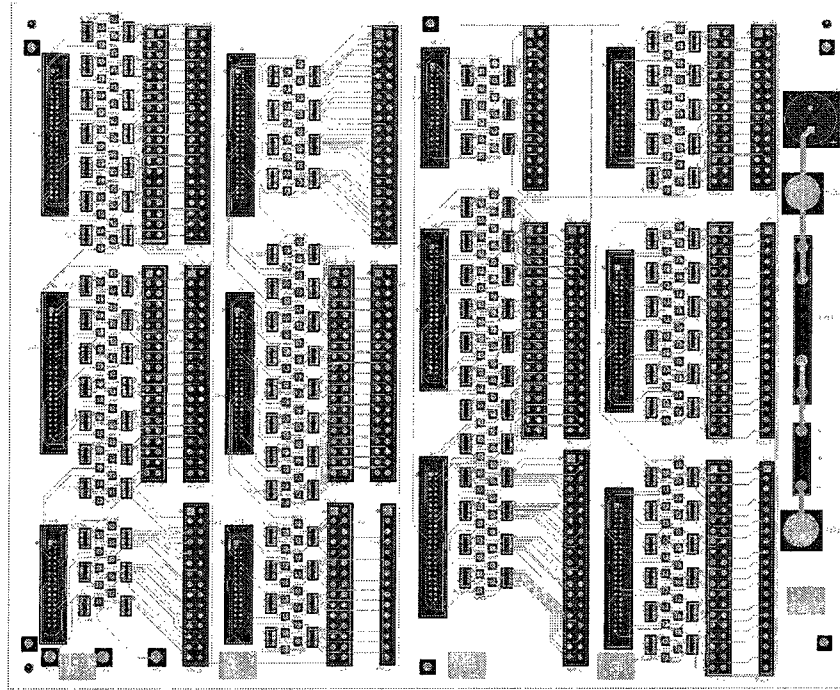
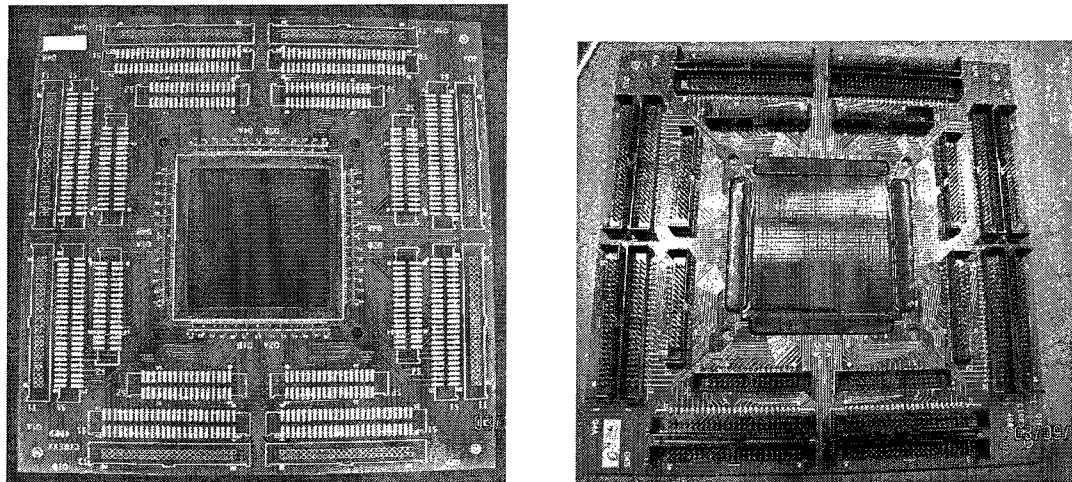


Figure B.6 : Screen capture of the 4-layer line driver circuit board in the Allegro Cadence PCB design software, showing only the components and their padstacks, and board dimensions.

Figure B.6 is a screen capture of the 4-layer line driver circuit board in Allegro Cadence. All files required for PCB fabrication and assembly are finalized unless the PCB design changes. Contact the CMC Lab at Rice University for free download of the Allegro software.

Suggestion: For PCB fabrication, Cirexx International has reasonable price and fast turn-around time. For PCB assembly, Houstech, Inc. charges the least but be prepared for extra time for repair. Suntronix, Inc. has the most advanced technology such as flying probe test to ensure good connections and no loose connections, but can charge twice as expensive as Houstech, Inc.



(a) SLM circuit board

(b) SLM board (with components)

Figure B.7 : (a) The SLM circuit board has a $34 \text{ mm} \times 34 \text{ mm}$ square hole surrounded by 1040 gold bond fingers, designed to mount and to wire-bond the SLM chip. (b) Besides the SLM chip, the SLM circuit board also has 24 cable connectors which receives voltage-amplified control signals from the line driver circuit.

B.5 SLM board

The SLM board is the interface between the SLM control circuit and the SLM chip, designed to fit the constraints in the wire-bonding procedures and to move around easily while conducting experiments.

As shown in Figure B.7, the SLM board, $4.5'' \times 4.5''$ in size and 40-mil thick, has a $34 \text{ mm} \times 34 \text{ mm}$ square hole in the middle, surrounded by 260 gold bond fingers on each side of the square. Each bond fingers are $5 \text{ mils} \times 20 \text{ mils}$ and are electroplated with 60 microinches of soft bondable gold. Four $4\text{-}40$ screw holes at the four corners of the square hole are useful for fixing the board in position during wire-bonding, and for an add-on transparent plastic case for chip protection. The distance from one side of the square hole to the edge of the board is around $1.5''$, which must be

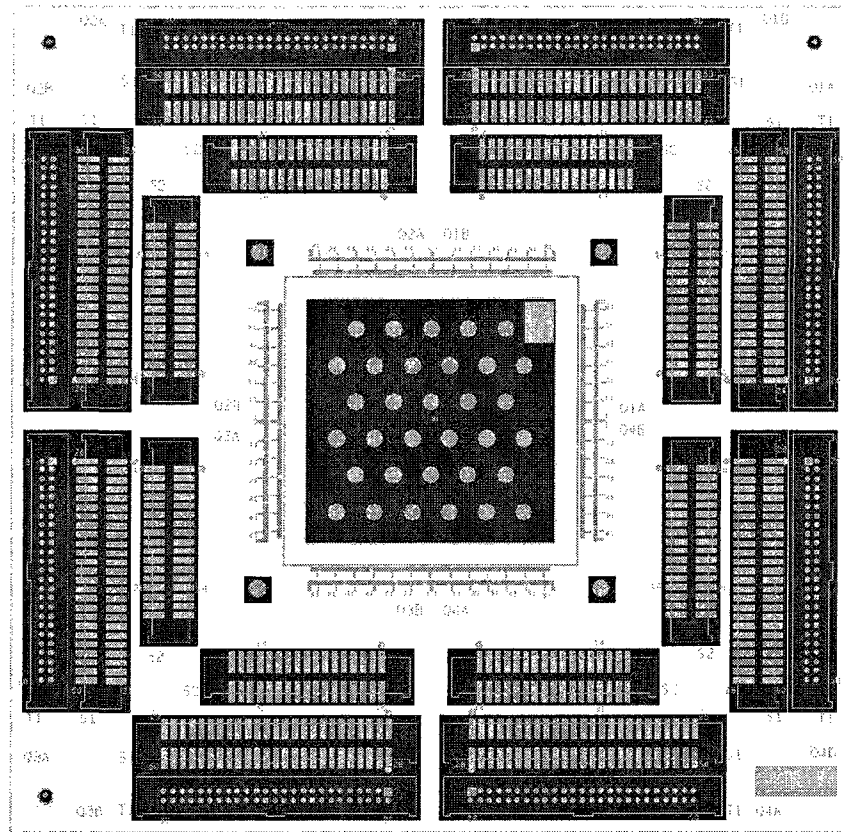
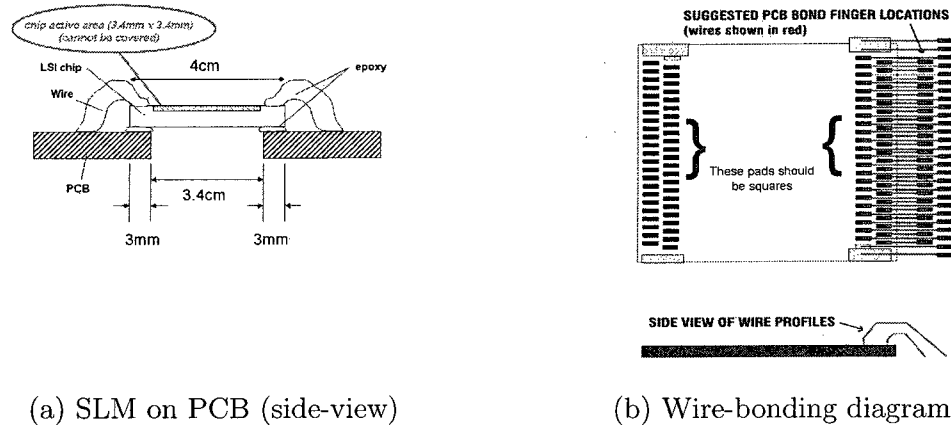


Figure B.8 : Screen capture of the top layer of the 4-layer SLM circuit board in the Cadence PCB design software, showing partially the wire connections among the various components. The middle upper layer is the ground plane, while the middle lower layer is the power plane.

shorter than the 2"-transducer arm of the wire-bonding machine. The height of the cable connectors are less than 6 mm so that they do not obstruct the transducer arm during wire-bonding. Any on-board components need to be at least 1.25 mm from the bond fingers.

The layout design procedures of the SLM board is the same as described in Section B.4, using the Allegro Design Entry CIS schematics software and the Allegro Cadence PCB layout software. See an example of the screen capture in Allegro Ca-



(a) SLM on PCB (side-view)

(b) Wire-bonding diagram

Figure B.9 : *Diagrams of SLM board showing how the SLM chip is mounted and wire-bonded onto the PCB (side-view (a) and top-view (b)).*

dence in Figure B.8. The white silkscreen labels on the SLM board helps identify its orientation and locate individual bond fingers (see Figure B.7).

Figure B.9 and B.10 are some diagrams sent to the wire-bonding company, VLSIP Technologies, Inc., for their reference. The company first attaches the SLM chip onto the PCB using Ablebond 84-3MV non-conductive epoxy on the 3mm-wide area between the chip and the board (see Figure B.9(a)). This die attach epoxy can withstand up to 425°C. Fixed on a 4.5" × 4.5" workholder with four 4-40 screws, the KnS 1488L Turbo wire-bonding machine places 1.3-mil 99.99% pure gold wires between each bond pad and PCB bond finger as in Figure B.9(b). The wire-bonding temperatures is 150°C and the length of each bond wire must be in between 50 mils and 150 mils, thus constraining the distance between the outer bond pads and outer bond fingers. To protect the wire bonds, the final procedure fills up the gap between the bond wires with a liquid encapsulant called Hysol[®] FP4450.

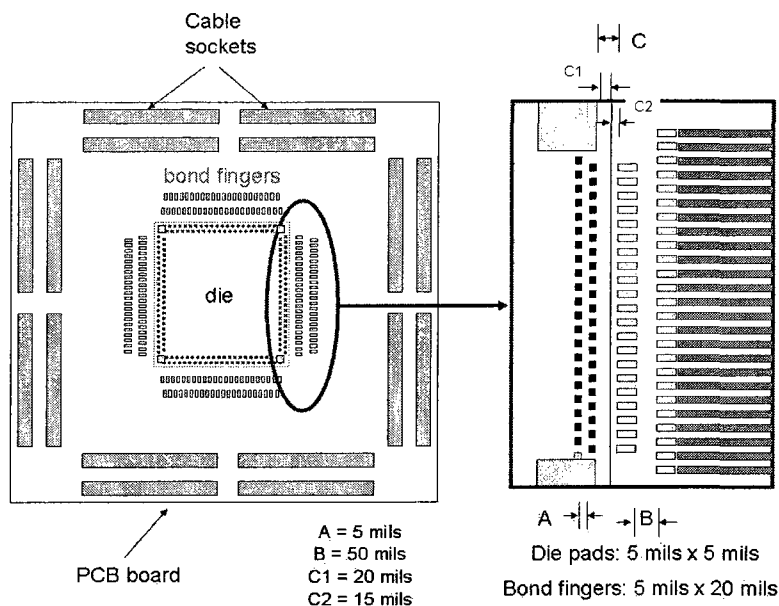
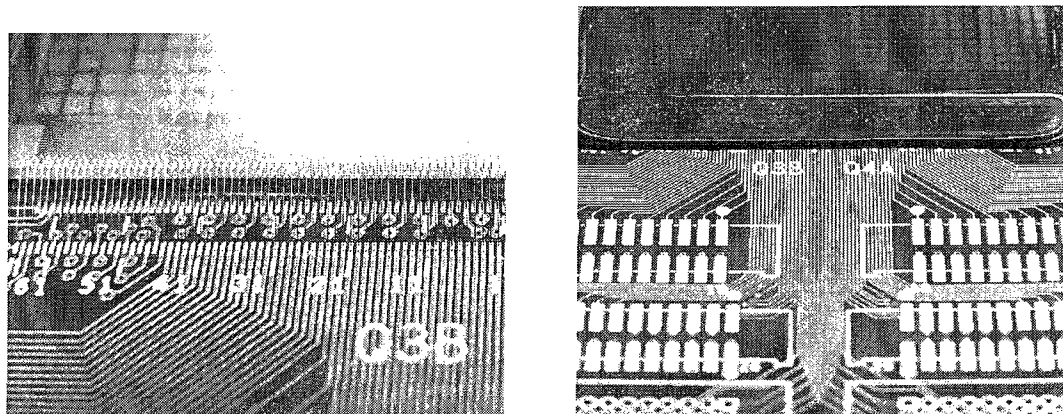


Figure B.10 : Detailed diagram near the square hole on the SLM board, with dimensions of the PCB bond fingers, and of the bond pads (schottky and ohmic contacts) of the SLM chip. Careful choices of the dimensions of bond pads and bond fingers, and the distances among them ensure successful wire-bonding.

Due to the special requirements in this project, the company requires 5 additional chips and boards for practice purpose. They successfully make all 1040 wire connections using the first practice chip, and subsequently bond all wires for the two SLM chips, missing only one wire. Figure B.11 displays some microscope images of the wire bonds on one side of the chip.

For more information about the wire-bonding, contact Nicholas Moses from VL-SIP Technologies, Inc.

Suggestion: The thicker the SLM board, the more external force it can withstand, thus providing more protection of the attached SLM chip. Recommended thickness:



(a) Gold wires connecting SLM to PCB

(b) Wire encapsulation

Figure B.11 : *Microscope images of the wire-bonded SLM chip from VLSIP Technologies, Inc., showing the 1-mil gold wires between the die pads and the gold bond fingers on the SLM board before and after encapsulating the wires with Hysol[®] FP4450.*

100 mils. Cracks later observed on the attached SLM chips after wire-bonding bring attention to the need for better chip protection (see Section 5.6).

B.6 Auxiliary components

The SLM control system uses a Mastech HY3005D-3 power supply to provide a 5V input to the FPGA circuit and a 16V input to the line driver circuit. The maximum current drawn from the 16V power supply is around 0.5A when all SLM pixels are biased. The FPGA circuit receives a clock input from a Simpson 420 function generator. Monitored on a Tektronix TDS3054 digital oscilloscope, the system always ensure synchronization between the pixel switching signals and the output trigger signal to the T-ray system. Always remember to set the oscilloscope as DC-coupled, instead of AC-coupled, for proper operation.

Cables and connectors are purchased from Samtec, Inc. The control system the

FPGA circuit to the line driver circuits using 15-pin and 25-pin IDSD cables, with 0.1" pin-to-pin separation, and TSW connectors. The SHF cable connectors and FFSD cables for connection between the line driver circuits and the SLM board are smaller in size, with only 0.05" pin-to-pin separation.

Caution: The FFSD cable headers break easily when disconnecting from the SHF connectors, once they are soldered onto the PCB. Always use a small flat-head screw driver and unplug the cables by piling the screw driver in the gap between the cable header and the connector. FTSH or FTS connectors are preferred over SHF in future designs.

Suggestion: FFSD cable length should be at least 40" for more flexible movement of the SLM board during experiment.

B.7 Synchronization with T-ray system

Every time the control system changes the pattern on the SLM, it needs to trigger the T-ray system to acquire a new waveform. This synchronization between the SLM and the waveform acquisition requires the time sequencing option implemented in the picometrix T-ray 4000 system. First, connect the trigger output of the FPGA circuit to the SYNC IN connector at the back of the T-ray 4000 control box using a BNC cable. The trigger signal needs to be a 5V TTL level pulse. Our system has a voltage amplifier circuit similar to the one in Figure B.5, which converts the trigger output of the FPGA circuit from 2.5V to 5V. Also, the system cannot detect any trigger signal with pulse width smaller than 250 μ s. Then, under the Tools Menu of the T-ray 4000 software, choose Time Sequencing. Always choose "extrn sync" in the pulldown

menu. Specify the number of averages, the number of waveforms desired to acquire, the file format and destination. Once the time sequence starts, the software saves one waveform named “Wfm1”, which should be discarded later. Afterwards, the system acquires a new waveform at every *fall* edge of the trigger signal.

Acquisition of each waveform in the T-ray 4000 system takes 10ms, thus the maximum acquisition speed for the T-ray 4000 system is 100Hz (better use 50Hz because of potential problems in software). For acquisition speed less than 10Hz, the .picotd text file format or TDMS format can be used. Acquisition at higher rate should use the picostream format, which can be converted to .picotd format under the software File menu. Always ensure proper acquisition by setting the trigger period 10ms longer than the total time required for signal averaging. For example, 100 signal averages would require the trigger period to be more than 1s.

More questions about synchronization with the T-ray 4000 system should be directed to Chris Megdanoff from Picometrix, LLC.

Caution: The frequency of the output trigger signal from the FPGA circuit always equals to the input clock frequency divided by 256. See implemented Verilog programs for more details.

B.8 System test procedure

All SLM experiments, including the SLM characterization experiments described in the Section 5.5 or any future imaging experiments, require proper operation of the SLM control system. Here briefly describes the procedure of testing the system for a typical experiment.

1. Turn on the power supply, the signal generator and the oscilloscope.

2. Turn on the switch on the FPGA AFX platform.
3. Open the ISE Impact software, and program the FPGA with the appropriate bitstream.
4. Observe the FPGA pin outputs and trigger signal on the oscilloscope to ensure correct voltage and signal timing (may need to press the reset button on the FPGA circuit to start, depending on the Verilog program).

Bibliography

- [1] W. L. Chan, J. Deibel, and D. M. Mittleman, “Imaging with terahertz radiation,” *Rep. Prog. Phys.*, vol. 70, pp. 1325–1379, 2007.
- [2] D. Zimdars, “High speed terahertz reflection imaging,” *Proc. SPIE*, vol. 5692, no. 1, pp. 255–259, 2005.
- [3] A. W. M. Lee, Q. Qin, S. Kumar, B. S. Williams, Q. Hu, and J. L. Reno, “Real-time terahertz imaging over a standoff distance (≥ 25 meters),” *Appl. Phys. Lett.*, vol. 89, p. 141125, 2006.
- [4] Z. Jiang and X.-C. Zhang, “Terahertz imaging via electrooptic effect,” *IEEE Trans. Microwave Th. Tech.*, vol. 47, pp. 2644–2650, 1999.
- [5] J. Pearce, H. Choi, D. M. Mittleman, J. White, and D. Zimdars, “Terahertz wide aperture reflection tomography,” *Opt. Lett.*, vol. 30, pp. 1653–1655, 2005.
- [6] S. Wang and X. Zhang, “Pulsed terahertz tomography,” *J. Phys. D: Appl. Phys.*, vol. 37, no. 964, pp. R31–R36, 2004.
- [7] A. Bandyopadhyay, A. Stepanov, B. Schulkin, M. D. Federici, A. Sengupta, D. Gary, J. F. Federici, R. Barat, Z.-H. Michalopoulou, and D. Zimdars, “Terahertz interferometric and synthetic aperture imaging,” *J. Opt. Soc. Am. A*, vol. 23, pp. 1168–1178, 2006.

- [8] D. Donoho, "Compressed sensing," *IEEE Trans. on Information Theory*, vol. 52, no. 4, pp. 1289–1306, 2006.
- [9] E. Candes, J. Romberg, and T. Tao, "Robust uncertainty principles: Exact signal reconstruction from highly incomplete frequency information," *IEEE Trans. on Information Theory*, vol. 52, no. 2, pp. 489–509, 2006.
- [10] M. F. Duarte, M. A. Davenport, D. Takhar, J. Laska, T. Sun, K. F. Kelly, and R. G. Baraniuk, "Single-pixel imaging via compressive sampling," *IEEE Sig. Proc. Mag.*, vol. 25, pp. 83–91, March 2008.
- [11] H.-T. Chen, W. J. Padilla, J. M. O. Zide, A. C. Gossard, A. J. Taylor, and R. D. Averitt, "Active terahertz metamaterial devices," *Nature*, vol. 444, pp. 597–600, 2006.
- [12] H.-T. Chen, W. J. Padilla, M. J. Cich, A. K. Azad, R. D. Averitt, and A. J. Taylor, "A metamaterial solid-state terahertz phase modulator," *Nat. Photonics*, vol. 3, p. 148, 2009.
- [13] D. H. Auston and K. P. Cheung, "Coherent time-domain far-infrared spectroscopy," *J. Opt. Soc. Am. B*, vol. 2, pp. 606–612, 1985.
- [14] P. R. Smith, D. H. Auston, and M. C. Nuss, "Subpicosecond photoconducting dipole antennas," *IEEE J. Quant. Elec.*, vol. 24, no. 2, pp. 255–260, 1988.
- [15] C. Fattinger and D. Grischkowsky, "Terahertz beams," *Appl. Phys. Lett.*, vol. 54, p. 490, 1989.
- [16] B. B. Hu and M. C. Nuss, "Imaging with terahertz waves," *Opt. Lett.*, vol. 20, pp. 1716–1719, 1995.

- [17] D. M. Mittleman, R. H. Jacobsen, and M. C. Nuss, "T-ray imaging," *IEEE Sel. Top. Quant. Elec.*, vol. 2, pp. 679–692, 1996.
- [18] D. Mittleman, *Sensing with Terahertz Radiation*. Springer Series in Optical Sciences, Heidelberg: Springer-Verlag, 2002.
- [19] M. van Exter and D. Grischkowsky, "Characterization of an optoelectronic terahertz beam system," *IEEE Trans. Microwave Th. Tech.*, vol. 38, no. 11, pp. 1684–1691, 1990.
- [20] P. U. Jepsen, R. H. Jacobsen, and S. R. Keiding, "Generation and detection of terahertz pulses from biased semiconductor antennas," *J. Opt. Soc. Am. B*, vol. 13, no. 11, pp. 2424–2436, 1996.
- [21] P. Y. Han and X.-C. Zhang, "Free-space coherent broadband terahertz time-domain spectroscopy," *Meas. Sci. Tech.*, vol. 12, pp. 1747–1756, 2001.
- [22] M. van Exter, C. Fattinger, and D. Grischkowsky, "High-brightness terahertz beams characterized with an ultrafast detector," *Appl. Phys. Lett.*, vol. 55, pp. 337–339, 1989.
- [23] Q. Wu and X.-C. Zhang, "Free-space electro-optic sampling of terahertz beams," *Appl. Phys. Lett.*, vol. 67, pp. 3523–3525, 1995.
- [24] A. Nahata, A. S. Weling, and T. F. Heinz, "A wideband coherent terahertz spectroscopy system using optical rectification and electro-optic sampling," *Appl. Phys. Lett.*, vol. 69, pp. 2321–2323, 1996.
- [25] C. Winnewisser, P. U. Jepsen, M. Schall, V. Schyja, and H. Helm, "Electro-optic detection of thz radiation in litao3, linbo3, and znte," *Appl. Phys. Lett.*, vol. 70,

- pp. 3069–3071, 1997.
- [26] P. Jepsen and B. M. Fischer, “Dynamic range in terahertz time-domain transmission and reflection spectroscopy,” *Opt. Lett.*, vol. 30, pp. 29–31, 2005.
 - [27] M. van Exter, C. Fattinger, and D. Grischkowsky, “Terahertz time-domain spectroscopy of water vapor,” *Opt. Lett.*, vol. 14, pp. 1128–1130, 1989.
 - [28] Q. Wu, T. D. Hewitt, and X.-C. Zhang, “Two-dimensional electro-optic imaging of thz beams,” *Appl. Phys. Lett.*, vol. 69, pp. 1026–1028, 1996.
 - [29] Q. Wu, F. G. Sun, P. Campbell, and X.-C. Zhang, “Dynamic range of an electro-optic field sensor and its imaging applications,” *Appl. Phys. Lett.*, vol. 68, pp. 3224–3226, 1996.
 - [30] J. Xu and X.-C. Zhang, “Circular involute stage,” *Opt. Lett.*, vol. 29, pp. 2082–2084, 2004.
 - [31] C. Janke, M. Forst, M. Nagel, H. Kurz, and A. Bartels, “Asynchronous optical sampling for high-speed characterization of integrated resonant terahertz sensors,” *Opt. Lett.*, vol. 30, pp. 1405–1407, 2005.
 - [32] T. Yasui, E. Saneyoshi, and T. Araki, “Asynchronous optical sampling terahertz time-domain spectroscopy for ultrahigh spectral resolution and rapid data acquisition,” *Appl. Phys. Lett.*, vol. 87, p. 061101, 2005.
 - [33] A. W. M. Lee and Q. Hu, “Real-time, continuous-wave terahertz imaging by use of a microbolometer focal-plane array,” *Opt. Lett.*, vol. 30, pp. 2563–2565, 2005.
 - [34] M. Herrmann, M. Tani, and K. Sakai, “Display modes in time-resolved terahertz imaging,” *Jap. J. Appl. Phys., Pt. 1*, vol. 39, pp. 6254–6258, 2000.

- [35] Z. Jiang and X.-C. Zhang, "2d measurement and spatio-temporal coupling of few-cycle thz pulses," *Opt. Express*, vol. 5, no. 11, pp. 243–248, 1999.
- [36] Z. Jiang and X.-C. Zhang, "Single-shot spatiotemporal terahertz field imaging," *Opt. Lett.*, vol. 23, pp. 1114–1116, 1998.
- [37] Z. Jiang and X.-C. Zhang, "Measurement of spatio-temporal terahertz field distribution by using chirped pulse technology," *IEEE J. Quant. Elec.*, vol. 36, pp. 1214–1222, 2000.
- [38] F. G. Sun, Z. Jiang, and X.-C. Zhang, "Analysis of terahertz pulse measurement with a chirped probe beam," *Appl. Phys. Lett.*, vol. 73, pp. 2233–2235, 1999.
- [39] G. Spickermann, F. Friederich, H. G. Roskos, and P. H. Bolivar, "High signal-to-noise-ratio electro-optical terahertz imaging system based on an optical demodulating detector array," *Opt. Lett.*, vol. 34, no. 21, pp. 3424–3426, 2009.
- [40] T. S. Hartwick, D. T. Hodges, D. H. Baker, and F. B. Foote, "Far infrared imagery," *Appl. Opt.*, vol. 15, pp. 1919–1922, 1976.
- [41] P. K. Cheo, "Far-infrared laser system for detection of defects in polyethylene-insulated power cables," *Opt. Lett.*, vol. 2, pp. 42–44, 1978.
- [42] A. Nahata, J. T. Yardley, and T. F. Heinz, "Free-space electro-optic detection of continuous-wave terahertz radiation," *Appl. Phys. Lett.*, vol. 75, pp. 2524–2526, 1999.
- [43] A. Nahata, J. T. Yardley, and T. F. Heinz, "Two-dimensional imaging of continuous-wave terahertz radiation using electro-optic detection," *Appl. Phys. Lett.*, vol. 81, pp. 963–965, 2002.

- [44] T. Lffler, T. May, C. a. Weg, A. Alcin, B. Hils, and H. G. Roskos, “Continuous-wave terahertz imaging with a hybrid system,” *Appl. Phys. Lett.*, vol. 90, p. 091111, 2007.
- [45] A. Galvanauskas, J. A. Tellefsen, A. Krotkus, M. Oberg, and B. Broberg, “Real-time picosecond electro-optic oscilloscope technique using a tunable semiconductor laser,” *Appl. Phys. Lett.*, vol. 60, pp. 145–147, 1992.
- [46] A. W. M. Lee, B. S. Williams, S. Kumar, Q. Hu, and J. L. Reno, “Real-time imaging using a 4.3-thz quantum cascade laser and a 320x240 microbolometer focal-plane array,” *IEEE Photonics Tech. Lett.*, vol. 18, pp. 1415–1417, 2006.
- [47] M. A. Belkin, F. Capasso, F. Xie, A. Belyanin, M. Fischer, A. Wittman, and J. Faist, “Room temperature terahertz quantum cascade laser source based on intracavity difference-frequency generation,” *Appl. Phys. Lett.*, vol. 92, no. 201101, 2008.
- [48] N. Karpowicz, H. Zhong, C. Zhang, K.-I. Lin, J.-S. Hwang, J. Xu, and X.-C. Zhang, “Compact continuous-wave subterahertz system for inspection applications,” *Appl. Phys. Lett.*, vol. 86, p. 054105, 2005.
- [49] Y. C. Shen, T. Lo, P. F. Taday, B. E. Cole, W. R. Tribe, and M. C. Kemp, “Detection and identification of explosives using terahertz pulsed spectroscopic imaging,” *Appl. Phys. Lett.*, vol. 86, p. 241116, 2005.
- [50] T. Yasuda, T. Iwata, T. Araki, and T. Yasui, “Improvement of minimum paint film thickness for thz paint meters by multiple-regression analysis,” *Appl. Opt.*, vol. 46, no. 30, pp. 7518–7526, 2007.

- [51] N. Karpowicz, H. Zhong, K.-I. Lin, J.-S. Hwang, and X. Zhang, “Comparison between pulsed terahertz time-domain imaging and continuous wave terahertz imaging,” *Semiconductor Sci. Tech.*, vol. 20, p. S293, 2005.
- [52] K. Kawase, Y. Ogawa, and Y. Watanabe, “Non-destructive terahertz imaging of illicit drugs using spectral fingerprints,” *Opt. Express*, vol. 11, pp. 2549–2554, 2003.
- [53] E. Pickwell and V. P. Wallace, “Biomedical applications of terahertz technology,” *J. Phys. D: Appl. Phys.*, vol. 39, pp. R301–R310, 2006.
- [54] J. B. Jackson, M. Mourou, J. F. Whitaker, I. N. Duling III, S. L. Williamson, M. Menu, and G. A. Mourou, “Terahertz imaging for non-destructive evaluation of mural paintings,” *Opt. Comm.*, vol. 281, no. 4, pp. 527–532, 2008.
- [55] S. Chen, D. Donoho, and M. Saunders, “Atomic decomposition by basis pursuit,” *SIAM J. Sci. Comp.*, vol. 20, no. 1, pp. 22–61, 1998.
- [56] R. G. Baraniuk, “Compressive sensing,” *IEEE Sig. Proc. Mag.*, vol. 24, no. 4, pp. 118–121, 2007.
- [57] E. van den Berg and M. P. Friedlander, “Probing the pareto frontier for basis pursuit solutions,” *SIAM J. on Sci. Comp.*, vol. 31, no. 2, pp. 890–912, 2008.
- [58] Y. Wang, J. Yang, W. Yin, and Y. Zhang, “A new alternating minimization algorithm for total variation image reconstruction,” *SIAM J. Imag. Sci.*, vol. 1, no. 3, pp. 248–272, 2008.
- [59] E. Candes, “Compressive sampling,” *Proc. Int. cong. Mathematicians*, vol. 3, pp. 1433–1452, 2006.

- [60] D. Takhar, J. Laska, M. Wakin, M. Duarte, D. Baron, S. Sarvotham, K. Kelly, and R. Baraniuk, "A new compressive imaging camera architecture using optical-domain compression," *Proc. SPIE*, vol. 6065, p. 606509, 2006.
- [61] M. E. Gehm, R. John, D. J. Brady, R. M. Willett, and T. J. Schulz, "Single-shot compressive spectral imaging with a dual-disperser architecture," *Opt. Express*, vol. 15, no. 21, pp. 14013–14027, 2007.
- [62] D. J. Brady, K. Choi, D. L. Marks, R. Horisaki, and S. Lim, "Compressive holography," *Opt. Express*, vol. 17, pp. 13040–13049, 2009.
- [63] F. J. Herrmann, Y. A. Erlangga, and T. T. Y. Lin, "Compressive simultaneous full-waveform simulation," *Geophys.*, vol. 74, no. 4, p. A35, 2009.
- [64] B. Jafarpour, V. K. Goyal, D. B. McLaughlin, and W. T. Freeman, "Transform-domain sparsity regularization of inverse problems in geosciences," *Geophys.*, vol. 74, no. 5, p. R69, 2009.
- [65] M. Lustig, D. Donoho, and J. M. Pauly, "Sparse mri: The application of compressed sensing for rapid mr imaging," *Magnetic Resonance in Medicine*, vol. 58, no. 6, pp. 1182–1195, 2007.
- [66] J. Provost and F. Lesage, "The application of compressed sensing for photoacoustic tomography," *IEEE Trans. Med. Imaging*, vol. 28, no. 4, pp. 585–594, 2009.
- [67] J. R. Fienup, "Reconstruction of an object from the modulus of its fourier transform," *Opt. Lett.*, vol. 3, no. 1, pp. 27–29, 1978.

- [68] M. T. Reiten, S. A. Harmon, and R. A. Cheville, "Terahertz beam propagation measured through three-dimensional amplitude profile determination," *J. Opt. Soc. Am. B*, vol. 20, no. 10, pp. 2215–2225, 2003.
- [69] M. L. Moravec, J. K. Romberg, and R. G. Baraniuk, "Compressive phase retrieval," *Proc. SPIE*, vol. 6701, p. 670120, 2007.
- [70] A. Chakraborti and B. Chakrabarti, "The travelling salesman problem on randomly diluted lattices: Results for small-size systems," *Eur. Phys. J. B*, vol. 16, pp. 677–680, 2000.
- [71] J. Xu and X. Zhang, "Terahertz wave reciprocal imaging," *Appl. Phys. Lett.*, vol. 88, p. 151107, 2006.
- [72] Z. Xu, W. L. Chan, D. M. Mittleman, and E. Y. Lam, "Sparse reconstruction of complex signals in compressed sensing terahertz imaging," *Signal Recovery and Synthesis, OSA Technical Digest (CD) (Optical Society of America, 2009)*, p. STuA4, 2009.
- [73] C. Li, *An Efficient Algorithm For Total Variation Regularization with Applications to the Single Pixel Camera and Compressive Sensing*. Master thesis, Rice University, 2009.
- [74] B. Ferguson and X.-C. Zhang, "Materials for terahertz science and technology," *Nat. Materials*, vol. 1, pp. 26–33, 2002.
- [75] P. H. Siegel, "Terahertz technology," *IEEE Trans. Microwave Th. Tech.*, vol. 50, pp. 910–928, 2002.

- [76] U. Efron, *Spatial Light Modulator Technology: Materials, Devices and Applications*. U.S.A.: CRC Press, 1995.
- [77] D. Engstrom, J. Bengtsson, E. Eriksson, and M. Goksor, “Improved beam steering accuracy of a single beam with a 1d phase-only spatial light modulator,” *Opt. Express*, vol. 16, p. 18275, 2008.
- [78] D. Dudley, W. Duncan, and J. Slaughter, “Emerging digital micromirror device (dmd) applications,” *Proc. SPIE*, vol. 4985, pp. 14–25, 2003.
- [79] T. Kleine-Ostmann, K. Pierz, G. Hein, P. Dawson, and M. Koch, “Audio signal transmission over thz communication channel using semiconductor modulator,” *Elec. Lett.*, vol. 40, pp. 124–126, 2004.
- [80] C. Jastrow, K. Munter, R. Piesiewicz, T. Kurner, M. Koch, and T. Kleine-Ostmann, “300 ghz transmission system,” *Elec. Lett.*, vol. 44, pp. 213–214, 2008.
- [81] J. W. Goodman, *Introduction to Fourier Optics*. U.S.A.: Roberts and Company Publishers, 2004.
- [82] R. Kersting, G. Strasser, and K. Unterrainer, “Terahertz phase modulator,” *Electron. Lett.*, vol. 36, pp. 1156–1158, 2000.
- [83] I. H. Libon, S. Baumgartner, M. Hempel, N. E. Hecker, J. Feldmann, M. Koch, and P. Dawson, “An optically controllable terahertz filter,” *App. Phys. Lett.*, vol. 76, pp. 2821–2823, 2000.
- [84] T. Kleine-Ostmann, P. Dawson, K. Pierz, G. Hein, and M. Koch, “Room-temperature operation of an electrically driven terahertz modulator,” *App. Phys. Lett.*, vol. 84, pp. 3555–3557, 2004.

- [85] P. Kuzel, F. Kaldec, J. Petzelt, J. Schubert, and G. Panaitov, "Highly tunable sr-tio₃/dysco₃ heterostructures for applications in the terahertz range," *App. Phys. Lett.*, vol. 91, p. 232911, 2007.
- [86] H.-T. Chen, S. Palit, T. Tyler, C. M. Bingham, J. M. O. Zide, J. F. O'Hara, D. R. Smith, A. C. Gossard, R. D. Averitt, W. J. Padilla, N. M. Jokerst, and A. J. Taylor, "Hybrid metamaterials enable fast electrical modulation of freely propagating terahertz waves," *App. Phys. Lett.*, vol. 93, p. 091117, 2008.
- [87] O. Paul, C. Imhof, B. Lagel, S. Wolff, J. Heinrich, S. Hofling, A. Forchel, R. Zengerle, R. Beigang, and M. Rahm, "Polarization-independent active metamaterial for high-frequency terahertz modulation," *Opt. Express*, vol. 17, p. 819, 2009.
- [88] A. K. Azad, A. J. Taylor, E. Smirnova, and J. F. O'Hara, "Characterization and analysis of terahertz metamaterials based on rectangular split-ring resonators," *App. Phys. Lett.*, vol. 92, p. 011119, 2008.
- [89] D. R. Smith, J. B. Pendry, and M. C. K. Wiltshire, "Metamaterials and negative refractive index," *Science*, vol. 305, p. 788, 2004.
- [90] J. B. Pendry, A. J. Holden, D. J. Robbins, and W. J. Stewart, "Magnetism from conductors and enhanced nonlinear phenomena," *IEEE Trans. Microwave Th. Tech.*, vol. 47, pp. 2075–2084, 1999.
- [91] J. B. Pendry, "Negative refraction makes a perfect lens," *Phys. Rev. Lett.*, vol. 85, pp. 3966–3969, 2000.
- [92] J. B. Pendry, D. Schurig, and D. R. Smith, "Controlling electromagnetic fields," *Science*, vol. 312, pp. 1780–1782, 2006.

- [93] U. Leonhardt, “Optical conformal mapping,” *Science*, vol. 312, pp. 1777–1780, 2006.
- [94] T. J. Yen, W. J. Padilla, N. Fang, D. C. Vier, D. R. Smith, J. B. Pendry, D. N. Basov, and X. Zhang, “Terahertz magnetic response from artificial materials,” *Science*, vol. 303, pp. 1494–1496, 2004.
- [95] “Compressive sensing resources,” <http://dsp.rice.edu/cs/>, 2010.
- [96] E. R. Brown, J. E. Bjarnason, A. M. Fedor, and T. M. Korter, “On the strong and narrow absorption signature in lactose at 0.53 thz,” *App. Phys. Lett.*, vol. 90, p. 061908, 2007.
- [97] K. H. Jin, Y. Kim, D.-S. Yee, O. K. Lee, and J. C. Ye, “Compressed sensing pulse-echo mode terahertz reflectance tomography,” *Opt. Lett.*, vol. 34, pp. 3863–3865, 2009.